

QUANTIFYING THE OBSERVATIONAL EFFORT REQUIRED FOR THE RADIAL VELOCITY CHARACTERIZATION OF TESS PLANETS

RYAN CLOUTIER^{1,2,3}, RENÉ DOYON³, FRANÇOIS BOUCHY⁴, AND GUILLAUME HÉBRARD⁵

Draft version July 4, 2018

ABSTRACT

The Transiting Exoplanet Survey Satellite will conduct a 2-year long wide-field survey searching for transiting planets around bright stars. Many TESS discoveries will be amenable to mass characterization via ground-based radial velocity measurements with any of a growing suite of existing and anticipated velocimeters in the optical and near-infrared. In this study we present an analytical formalism to compute the number of radial velocity measurements—and hence the total observing time—required to characterize RV planet masses with the inclusion of either a white or correlated noise activity model. We use our model to calculate the total observing time required to measure all TESS planet masses from the expected TESS planet yield while relying on our current understanding of the targeted stars, stellar activity, and populations of unseen planets which inform the expected radial velocity precision. We also present specialized calculations applicable to a variety of interesting TESS planet subsets including the characterization of 50 planets smaller than 4 Earth radii which is expected to take as little as 60 nights of observation. Although, the efficient RV characterization of such planets requires a-priori knowledge of the ‘best’ targets which we argue can be identified prior to the conclusion of the TESS planet search based on our calculations. Our results highlight the comparable performance of optical and near-IR spectrographs for most planet populations except for Earths and temperate TESS planets which are more efficiently characterized in the near-IR. Lastly, we present an online tool to the community to compute the total observing times required to detect any transiting planet using a user-defined spectrograph (*RVFC*).

1. INTRODUCTION

NASA’s *Transiting Exoplanet Survey Satellite* (TESS; [Ricker et al. 2015](#)) launched in April 2018, is conducting a wide-field survey over at least a 2-year long period and is expected to discover approximately 1700 new transiting exoplanet candidates at a 2-minute cadence around nearby stars over nearly the entire sky ([Sullivan et al. 2015](#), hereafter [S15](#)). Due to their proximity, many candidate TESS planetary systems, or TESS objects-of-interest (TOIs), will be amenable to precision radial velocity (RV) observations using ground-based velocimeters to establish their planetary nature and to measure the masses of identified planets. The population of TESS planets to-be discovered are on average systematically closer than the 2342 validated Kepler planets⁶ of which only 243 (~ 10%) have been characterized with RVs.

The growing number of precision velocimeters—and their variety—is vast and includes both optical and near-infrared spectrographs (APF; [Vogt et al. 2014](#), CARMENES; [Quirrenbach et al. 2014](#), CORALIE; ESPRESSO; [Pepe et al. 2010](#), EXPRES; [Jurgenson et al. 2016](#), G-CLEF; [Szentgyorgyi et al. 2016](#), GIANO; [Oliva](#)

[et al. 2006](#), GIARPS; [Claudi et al. 2016](#), HARPS; [Mayor et al. 2003](#), HARPS-N; [Cosentino et al. 2012](#), HARPS-3, HDS; [Noguchi et al. 1998](#); HIRES; [Vogt et al. 1994](#), HPF; [Mahadevan et al. 2012](#), IRD; [Kotani et al. 2014](#), iLocater; [Crepp et al. 2016](#), iSHELL, [Rayner et al. 2012](#), KPF; [Gibson et al. 2016](#), MAROON-X; [Seifahrt et al. 2016](#), MINERVA; [Swift et al. 2015](#), MINERVA-Red; [Sliski et al. 2017](#), NEID; [Allen et al. 2018](#), NIRPS; [Bouchy et al. 2017](#), NRES; [Sivard et al. 2016](#), PARAS; [Chakraborty et al. 2008](#), PARVI, PEPSI; [Strassmeier et al. 2015](#), PF5; [Crane et al. 2010](#), SALT HRS; [Crause et al. 2014](#), SOPHIE; [Perruchot et al. 2011](#), SPIROU; [Artigau et al. 2014](#), TOU; [Ge et al. 2016](#), Veloce, WISDOM; [Fűrész et al. 2016](#)). Given the large number of velocimeters that can be used for RV characterization of TESS planet masses it is useful to understand the observational effort required to do so. That is, how many radial velocity measurements—and total observing time—are required to detect the masses of the TESS planets at a given significance. Furthermore, it is critical to access which spectrographs are best-suited to the efficient mass characterization of each transiting planet found with TESS. To address these questions, here we present an analytical formalism to compute the number of RV measurements required to detect a transiting planet’s mass and apply it to the expected TESS planet yield from [S15](#). Combining these calculations with an exposure time calculator provides estimates of the total observing time required to measure all TESS planet masses and to complete a variety of interesting science cases that will be addressed by TESS.

This paper is structured as follows: [Sect. 2](#) describes our model used to compute the total observing time for all TESS objects-of-interest, [Sect. 3](#) compares our model

¹ Dept. of Astronomy & Astrophysics, University of Toronto, 50 St. George Street, Toronto, Ontario, M5S 3H4, Canada

² Centre for Planetary Sciences, Dept. of Physical & Environmental Sciences, University of Toronto Scarborough, 1265 Military Trail, Toronto, Ontario, M1C 1A4, Canada

³ Institut de recherche sur les exoplanètes, Département de physique, Université de Montréal, 2900 boul. douard-Montpetit, Montréal, Quebec, H3T 1J4, Canada

⁴ Observatoire Astronomique de l’Université de Genève, 51 Chemin des Maillettes, 1290 Versoix, Switzerland

⁵ Institut d’astrophysique de Paris

⁶ According to the NASA Exoplanet Archive accessed on March 18, 2018.

to results from existing RV follow-up campaigns of known transiting planetary systems, Sect. 4 describes the application of our model to the expected TESS planet population, and Sect. 5 reports the results for all TESS planets and for various science cases. We conclude with a discussion and conclusions in Sect. 6. Lastly, in the Appendix A we describe our freely available web-tool that utilizes the model from Sect. 2 to calculate the total observing time required to detect any transiting planet with a user-defined spectrograph.

2. MODELLING THE TOTAL OBSERVING TIME REQUIRED TO MEASURE A TRANSITING PLANET'S MASS

Here we derive equations to calculate the number of RV measurements N_{RV} , of an arbitrary star—in our case a TESS object-of-interest (TOI)—required to measure the mass of its transiting planet at a given detection significance; i.e. with a particular RV semi-amplitude measurement uncertainty σ_K . Together with calculations of the exposure time, N_{RV} can be used to compute the total observing time required to detect each TESS planet with RVs.

2.1. Calculating σ_K from the Fisher Information

Given an RV time-series of a TOI $\mathbf{y}(\mathbf{t})$ taken a times \mathbf{t} , the amount of information present in the data with regards to the value of the planet's RV semi-amplitude K is contained in the Fisher information. The amount of information regarding K is the K measurement uncertainty σ_K , that is calculated by evaluating the Fisher information given a model of the observed stellar RV variations due to the planet.

The Fisher information matrix B is defined as the Hessian matrix of the lnlikelihood of the data given a model where the model is parameterized by a set of n parameters $\boldsymbol{\theta} = \{\theta_1, \dots, \theta_n\}$. Explicitly,

$$B_{ij} = -\frac{\partial^2 \ln \mathcal{L}}{\partial \theta_i \partial \theta_j} \quad (1)$$

where the indices $i, j = 1, \dots, n$ and

$$\ln \mathcal{L} = -\frac{1}{2} [(\mathbf{y}(\mathbf{t}) - \boldsymbol{\mu}(\mathbf{t}))^T C^{-1} (\mathbf{y}(\mathbf{t}) - \boldsymbol{\mu}(\mathbf{t})) + \ln \det C + N_{\text{RV}} \ln 2\pi] \quad (2)$$

is the generalized lnlikelihood of $\mathbf{y}(\mathbf{t})$ given a model $\boldsymbol{\mu}(\mathbf{t})$. The RV time-series and model are each 1D vectors containing N_{RV} measurements. The matrix C is the $N_{\text{RV}} \times N_{\text{RV}}$ covariance matrix of the residual time-series $\mathbf{y}(\mathbf{t}) - \boldsymbol{\mu}(\mathbf{t})$. Once constructed, the Fisher information matrix can be inverted to return a new covariance matrix; the covariance matrix of the n model parameters and whose diagonal elements are equal to the measurement variances in the model parameters.

The model of observed stellar RV variations due to a single orbiting planet is a keplerian solution. Its general form is written as

$$\boldsymbol{\mu}(\mathbf{t}, P, T_0, K, e, \omega) = K[\cos(\boldsymbol{\nu}(\mathbf{t}, P, T_0, e, \omega) + \omega) + e \cos \omega], \quad (3)$$

in terms of the star's orbital period P , time of inferior conjunction T_0 , RV semi-amplitude K , orbital eccentricity e , argument of periapsis ω , and true anomaly $\boldsymbol{\nu}$. If we assume that the planet's orbit is circular—as was done in S15—then our keplerian model reduces to

$$\boldsymbol{\mu}(\mathbf{t}, P, T_0, K) = -K \sin \boldsymbol{\nu}(\mathbf{t}, P, T_0) \quad (4)$$

where the true anomaly can be expressed as $\boldsymbol{\nu}(\mathbf{t}, P, T_0) = 2\pi(\mathbf{t} - T_0)/P$.

2.1.1. Calculating σ_K with white RV noise

Using the keplerian model given in Eq. 4 we can derive a simple analytical expression for σ_K in terms of N_{RV} from the Fisher information under a few more simplifying assumptions. From the resulting expression one can fix σ_K to a desired measurement value and calculate N_{RV} required to measure K at that precision. As a initial assumption, where we will assume that the observed RV noise is Gaussian distributed, or white. This assumption is used in the majority of RV analyses in the literature and is especially applicable to planets with semi-amplitudes much greater than the measured point-to-point RV rms. Assuming white noise, the covariance matrix C in Eq. 2 is diagonal with RV measurement variances $\sigma_{\text{RV}}^2(\mathbf{t})$ along the diagonal. The resulting lnlikelihood reduces to

$$\ln \mathcal{L} = -\frac{1}{2} \sum_{i=1}^{N_{\text{RV}}} \left(\frac{y(t_i) - \mu(t_i)}{\sigma_{\text{RV}}(t_i)} \right)^2, \quad (5)$$

modulo a constant offset that is independent of the model parameters.

The second simplifying assumption is rather than considering the full measurement uncertainty time-series $\boldsymbol{\sigma}(\mathbf{t})$, we will assume that the RV measurement uncertainty is well-characterized over time by a scalar value σ_{RV} ; a common assumption when deriving model parameter uncertainties from time-series observations (e.g. Gaudi & Winn 2007; Carter et al. 2008). Thirdly, in our keplerian model we will assume that the values of P and T_0 are known a-priori with absolute certainty from the planet's TESS transit light curve. Although this is not strictly true, P and T_0 are often measured at high precision—compared to K —when multiple transit events are detected. Thus we can treat P and T_0 as constants rather than as model parameters such that the set of model parameters in our keplerian RV solution reduces to a single value; $\boldsymbol{\theta} = \{K\}$. The Fisher information matrix then reduces to the scalar value

$$B = -\frac{\partial^2 \ln \mathcal{L}}{\partial K^2}, \quad (6)$$

$$= \frac{1}{\sigma_{\text{RV}}^2} \sum_{i=1}^{N_{\text{RV}}} \sin^2 \nu(t_i, P, T_0), \quad (7)$$

$$= \frac{N_{\text{RV}}}{2\sigma_{\text{RV}}^2}, \quad (8)$$

where in the final step we have assumed that the N_{RV} measurements are uniformly sampled over the planet's orbital phases such that the summation term in Eq. 7 averages to one half of N_{RV} .

The inverse of the expression in Eq. 8 is the K measurement variance or

$$\sigma_K = \sigma_{\text{RV}} \sqrt{\frac{2}{N_{\text{RV}}}}. \quad (9)$$

This remarkably simple expression for σ_K as a function of the RV measurement uncertainty and number of RV measurements can be rearranged to calculate the value of N_{RV} that is required to detect K of any transiting planet, with a precision of σ_K , when the RV noise can be accurately treated as white.

2.1.2. Calculating σ_K when relaxing the white RV noise approximation

In deriving Eq. 9 we must assume that the RV time-series noise was Gaussian distributed. However, numerous analyses of transiting systems have shown that there exist cases in which this is a poor assumption. Instead the RV residuals—after the removal of planetary models—can be temporally correlated often owing to the presence of RV signals arising from stellar activity (e.g. Haywood et al. 2014; Grunblatt et al. 2015; López-Morales et al. 2016; Cloutier et al. 2017b; Dittmann et al. 2017). In such cases, a correlated ‘noise’⁷ model must be fit simultaneously with the planetary models to account for all suspected RV signals and any potential correlations between model parameters. One popular choice of correlated noise activity model is a Gaussian process (GP) regression model with a quasi-periodic covariance kernel of the form

$$k(t_i, t_j) = a^2 \exp \left[-\frac{(t_i - t_j)^2}{2\lambda^2} - \Gamma^2 \sin^2 \left(\frac{\pi |t_i - t_j|}{P_{\text{GP}}} \right) \right], \quad (10)$$

and covariance matrix elements

$$C_{ij} = k(t_i, t_j) + \delta_{ij} \sqrt{\sigma_{\text{RV}}^2(t_i) + \sigma_{\text{jitter}}^2}, \quad (11)$$

where t_i is the i^{th} observation epoch in \mathbf{t} and δ_{ij} is the Kronecker delta function. The covariance of the GP model function is parameterized by five hyperparameters: the amplitude of the correlations a , the exponential timescale λ , the coherence parameter Γ , the periodic timescale P_{GP} , and an additive scalar jitter σ_{jitter} . When attempting to measure the semi-amplitude of a known transiting planet, along with a quasi-periodic GP activity model, the full set of model parameters becomes $\boldsymbol{\theta} = \{K, a, \lambda, \Gamma, P_{\text{GP}}, \sigma_{\text{jitter}}\}$. Hence our new Fisher information matrix will be 6×6 and takes into account the dependence of the K measurement precision on the remaining hyperparameters.

The elements of the Fisher information matrix are computed identically as before from Eqs. 1 and 2 but now using a non-diagonal covariance matrix C (Eq. 11). The derivation of the elements of B are provided in Appendix B. The general effect of computing σ_K from this new Fisher information matrix is to decrease its expected value given a time-series of fixed N_{RV} compared to the

⁷ Note that we use the term correlated ‘noise’ whereas—if arising from temporally correlated stellar activity—then this is a signal rather than noise but it is not the planetary signal that we interested in.

value obtained when using Eq. 9. The resulting N_{RV} is typically larger than in the white noise limit. However unlike computing σ_K in the white noise limit, the value of σ_K when including a GP correlated noise activity model is dependent on the values of the model parameters themselves and on the time-series due to the $t_i - t_j$ terms in the covariance kernel (Eq. 10) and the appearance of $\mathbf{y}(\mathbf{t})$ and $\boldsymbol{\sigma}(\mathbf{t})$ in the likelihood such that

$$B \rightarrow B(\mathbf{t}, \mathbf{y}, \boldsymbol{\sigma}_{\text{RV}}, \boldsymbol{\theta}). \quad (12)$$

Therefore estimating σ_K from the Fisher information including correlated noise requires time-series as input and numerical values for all model parameters in $\boldsymbol{\theta}$.

We note that when including a GP correlated noise activity model, a simple analytical expression for σ_K in terms of σ_{RV} and N_{RV} cannot be derived. In this case σ_K must be derived as a function of N_{RV} from time-series of varying N_{RV} used to compute the full Fisher information using Eq. 1 before calculating the covariance matrix of the model parameters $C' = B^{-1}$ and ultimately σ_K from its corresponding diagonal matrix element:

$$\sigma_K = \sqrt{C'_{11}}. \quad (13)$$

2.2. Calculating σ_{RV} for TOIs in the photon-noise limit

Calculating σ_K from RV time-series with either white noise or correlated noise is dependent in-part on the RV measurement uncertainty. Here we estimate the photon-noise limited RV measurement precision σ_{RV} following the formalism from Bouchy et al. (2001). Their formalism is used to calculate σ_{RV} given the RV information content contained within a stellar spectrum over a particular wavelength range of interest.

From Bouchy et al. (2001) the RV measurement precision σ_{RV} is shown to be

$$\sigma_{\text{RV}} = \frac{c}{Q \cdot \text{S/N}}, \quad (14)$$

where c is the speed of light, Q is known as the quality factor of the spectrum, and S/N is the signal-to-noise ratio achieved over the full spectral range considered. The S/N contains contributions from the total number of photoelectrons N_{e^-} obtained from the source and a contribution from readout noise that begins to dominate the noise budget for the faintest TESS stars. Our S/N prescription is

$$\text{S/N} = \frac{N_{e^-}}{\sqrt{N_{e^-} + N_{\text{ron}}^2}}. \quad (15)$$

Throughout this study we assume a fixed readout noise per pixel of $5 e^-$ and a 4 pixel PSF sampling in each orthogonal direction on the detector. The corresponding readout noise is therefore $N_{\text{ron}} = 20 e^-$. The quality factor

$$Q = \frac{\sqrt{\sum_i W_i}}{\sqrt{\sum_i A_i}} \quad (16)$$

is calculated from the noise-free stellar spectrum A_i —given in photoelectrons and evaluated at the wavelengths

TABLE 1
ADOPTED SPECTRAL BANDS

Spectral Band	Central Wavelength [μm]	Effective Band Width [μm]	Zero-point Flux Density [erg/s/cm ² / μm]
<i>U</i>	0.3531	0.0657	3.678×10^{-5}
<i>B</i>	0.4430	0.0973	6.293×10^{-5}
<i>V</i>	0.5537	0.0890	3.575×10^{-5}
<i>R</i>	0.6940	0.2070	1.882×10^{-5}
<i>I</i>	0.8781	0.2316	9.329×10^{-6}
<i>Y</i>	1.0259	0.1084	5.949×10^{-6}
<i>J</i>	1.2545	0.1548	2.985×10^{-6}
<i>H</i>	1.6310	0.2886	1.199×10^{-6}
<i>K</i>	2.1498	0.3209	4.442×10^{-7}

NOTE. — Values presented here were obtained from the [SVO Filter Profile Service](#). Explicitly, values pertaining to any of the *UBVRI* bands were obtained from the Generic/Johnson filter set whereas the *YJHK* bands were obtained from the CFHT/Wircam filter set.

λ_i —and from the optimum weighting function given by

$$W_i = \left(\frac{\lambda_i^2}{A_i} \right) \left(\frac{\partial A_i}{\partial \lambda_i} \right)^2. \quad (17)$$

The quality factor represents the density of the RV information content in the spectrum A_i .

When computing σ_{RV} from Eq. 14 we use model stellar spectra from the PHOENIX-ACES library (Husser et al. 2013). The spectrum for each TOI is retrieved based on the star’s effective temperature T_{eff} and surface gravity (see S15) assuming solar metallicity. The native cgs units of flux density for each model spectrum are converted to photoelectrons using the photon energy over the wavelength range provided by the PHOENIX models ($\lambda \in [0.05, 5.5] \mu\text{m}$) and assuming a fixed nominal instrumental throughput of 5%. The spectrum is then segregated into the spectrograph’s various spectral bands whose central wavelengths and spectral coverage are summarized in Table 1. In each spectral band we mask wavelengths at which the telluric transmission is $< 98\%$, where the spectral telluric absorption model is calculated at an airmass of 1 from Maunakea at $R = 100,000$. The aforementioned model is obtained from the TAPAS web-tool (Bertaux et al. 2014). The remaining spectrum in each band that is largely uncontaminated by telluric absorption is resampled assuming a fixed 3 pixel PSF sampling of each resolution element. This spectrum is then convolved with a Gaussian kernel whose full width at half maximum is $\text{FWHM} = \lambda_0/R$ where R is the spectral resolution of the spectrograph. After convolving each spectrum with a Gaussian instrumental profile the spectrum is convolved with the rotation kernel presented in Gray (2008) (c.f. Eq. 17.12) that emulates the effect of rotational broadening for stars with a non-zero projected rotation velocity $v \sin i_s$. When computing the rotation kernel we adopt a linear limb-darkening coefficient of $\epsilon = 0.6$. For each star we compute $v \sin i_s$ from the known stellar radius (see S15), the inclination of the stellar spin-axis to the line-of-sight i_s —drawn from a narrow geometric distribution centered on 90° —and the stellar rotation period P_{rot} , that we sample following the methodology described in Sect. 2.4.

After the aforementioned convolutions the PHOENIX

model’s wavelength grid is resampled to a constant $\delta\lambda = \lambda_0/R$ whose value is specified at the center of a reference band. For the optical spectrograph that will be considered in this study we fix the reference band to be the *V* band ($\lambda_0 = 0.55 \mu\text{m}$) whereas the reference band is fixed to the *J* band ($\lambda_0 = 1.25 \mu\text{m}$) with the near-IR spectrograph considered.

Artigau et al. (2018) compared the value of σ_{RV} derived from stellar spectra—as we do here—to the value derived from empirical spectra from HARPS, ESPaDOnS, and CRIRES. They find small discrepancies between these values at optical wavelengths but claim that the RV precision derived from model spectra can be over-estimated in the near-IR YJ bands by ~ 2 and under-estimated in the HK bands by ~ 0.5 . In deriving our own RV measurement precisions from spectral models in the optical or near-IR, we apply the multiplicative correct factors derived in Artigau et al. (2018). We note that these corrections were derived based on observations of a single star (i.e. Barnard’s star) whereas the correction factors for other star’s with unique effective temperatures and metallicities may differ from those used here. Despite that, there exists a clear discrepancy between RV measurement precisions derived from model and empirical spectra. This is at least true in a subset of spectral bands. Precise disagreements between model and observationally-derived σ_{RV} in various bands for *all* spectral types is beyond the scope of this paper but may affect the photon-noise limited RV precision by a factor $\mathcal{O}(2)$ —depending on the spectrograph—as it does for Barnard’s star from the $\sim J$ to K band. Note that the corresponding effect on total observing times will be $\mathcal{O}(< 2)$ due to the other contributors to the RV uncertainty in addition to the photon-noise limit (see Sect. 2.3).

2.3. Additional sources of RV noise

Often when searching for transiting planets in radial velocity the residual rms following the removal of the maximum a-posteriori keplerian planet solution exceeds the characteristic RV measurement uncertainty. This implies the existence of additional sources of RV noise. The effect of these additional noise sources is detrimental to our ability to precisely measure planet masses if not properly modelled. Therefore this excess noise should be taken into account when attempting to estimate σ_K using either Eq. 9 or 13. These additional sources of noise may be attributed to stellar activity arising from dark spots, plages, and/or faculae, whose corresponding RV signals are modulated by the stellar rotation period and its harmonics, modulo the amplitude of any differential rotation (e.g. Forveille et al. 2009; Bonfils et al. 2013; Delfosse et al. 2013). Another source of dispersion in observed RVs may be from additional planets not seen in-transit (e.g. Christiansen et al. 2017; Cloutier et al. 2017b, Bonfils et al. in prep.); an effect that is especially pertinent when searching for small planets whose RV semi-amplitudes are less than the characteristic RV uncertainty of the time-series (e.g. Astudillo-Defru et al. 2017b).

In order to compute N_{RV} for each TOI using our white noise model we will absorb the aforementioned additional noise sources into an effective RV uncertainty σ_{eff} rather than the previously assumed measurement uncertainty derived in the photon-noise limit. The effec-

tive RV uncertainty is written as the quadrature sum of the systematic RV noise floor of the spectrograph σ_{floor} (see Table 4), the photon-noise limited RV precision, and the RV jitter arising from additional sources of RV noise such as activity and unknown planets: $\sigma_{\text{eff}} = \sqrt{\sigma_{\text{floor}}^2 + \sigma_{\text{RV}}^2 + \sigma_{\text{act}}^2 + \sigma_{\text{planets}}^2}$. Eq. 9 can then be rearranged for N_{RV} in terms of the effective RV uncertainty:

$$N_{\text{RV}} = 2 \left(\frac{\sigma_{\text{eff}}}{\sigma_{\text{K}}} \right)^2. \quad (18)$$

In empirical time-series with white RV residuals σ_{eff} can be estimated from the rms of the residual dispersion following the removal of all modelled planets. Eq. 18 is not applicable to empirical time-series that require a GP correlated noise activity model.

In Sect. 3 we will compare the results from real RV campaigns to our analytic estimates as a test of their validity. However unlike in actual RV time-series, the RV jitter rms resulting from activity and unknown planets is not known a-priori for any of the TOIs in the S15 synthetic catalog. We therefore need to employ generalized statistical arguments to estimate the expected RV jitter from activity and unknown planets for each TOI. These estimates are described in Sects. 2.4 and 2.5 and are based on the empirical distributions of RV jitter from each of these two physical effects.

2.4. Estimating RV noise due to stellar activity

Here we will consider estimates of the expected RV jitter due to rotationally modulated stellar activity; σ_{act} . The arguments presented here are intended to be representative of field stars in the solar neighbourhood. Firstly, for each TOI we draw a rotation period P_{rot} as a function of the stellar mass from either the Pizzolato et al. (2003) empirical distribution for FGK dwarfs ($T_{\text{eff}} > 3800$ K) or from the Newton et al. (2016) empirical distribution for M dwarfs ($T_{\text{eff}} \leq 3800$ K). The corresponding stellar equatorial velocity is calculated using the stellar radius from S15. The projected stellar rotation velocity $v \sin i_s$ is then calculated after drawing the inclination of the stellar spin-axis from a geometrical distribution. The value of $v \sin i_s$ acts as a first-order estimate of the star's activity level (e.g. West et al. 2015; Moutou et al. 2017).

For active stars ($P_{\text{rot}} \lesssim 10$ days), Oshagh et al. (2017) showed through simultaneous K2 photometry and HARPS spectroscopy that monotonic correlations exist between the measured RVs and numerous spectroscopic activity indicators (e.g. $\log R'_{\text{HK}}$, FWHM, BIS). Meanwhile quiet stars ($P_{\text{rot}} \gtrsim 10$ days) appear to lack such strong correlations with spectroscopic activity indicators yet do correlate strongly with F_8 , the photometric flicker or photometric RMS on timescales < 8 hours (Bastien et al. 2013). The F_8 parameter has been shown to correlate with asteroseismic stellar surface gravity measurements (Bastien et al. 2013) that itself correlates with RV jitter (Bastien et al. 2014). Thus for inactive FGK stars ($P_{\text{rot}} \geq 10$ days) we adopt the following temperature dependent relation from Cegla et al. (2014) for the expected

RV dispersion due to stellar activity:

$$\sigma_{\text{act}} = 1 \text{ ms}^{-1} \times \begin{cases} 84.23F_8 - 3.35, & T_{\text{eff}} \geq 6000 \text{ K}, \\ 18.04F_8 - 0.98, & T_{\text{eff}} < 6000 \text{ K}. \end{cases} \quad (19)$$

Typical values of σ_{act} used to derive Eq. 19 from Saar et al. (2003) range from $\sim 0.5 - 10 \text{ m s}^{-1}$ but with a relatively small median value of $\lesssim 2 \text{ m s}^{-1}$. We sample F_8 values—measured in parts-per-thousand—from the empirical *Kepler* distribution that has been corrected for their intrinsic *Kepler* magnitude (Bastien et al. 2013). After sampling F_8 and its uncertainty we use Eq. 19 to map to the distribution of σ_{act} for the inactive FGK stars in the sample of planet-hosting TOIs.

For active FGK stars ($P_{\text{rot}} < 10$ days) we revert to the $\log R'_{\text{HK}}$ activity indicator (Noyes et al. 1984) whose distribution among nearby field FGK stars has been well-characterized (Henry et al. 1996; Santos et al. 2000; Wright et al. 2004; Hall et al. 2007; Isaacson & Fischer 2010; Lovis et al. 2011). To estimate σ_{act} for active FGK stars we compute the corresponding $\log R'_{\text{HK}}$ from P_{rot} and $B - V$ using the formalism from Noyes et al. (1984). The following formulation from Santos et al. (2000) is then used to map $\log R'_{\text{HK}} \rightarrow \sigma_{\text{act}}$:

$$\sigma_{\text{act}} = 1 \text{ ms}^{-1} \times \begin{cases} 9.2R_5^{0.75} & \text{for F dwarfs} \\ 7.9R_5^{0.55} & \text{for G dwarfs} \\ 7.8R_5^{0.13} & \text{for K dwarfs,} \end{cases} \quad (20)$$

where $R_5 = 10^5 R'_{\text{HK}}$. The rms of the fits in Eq. 20 are 0.17, 0.18, and 0.19 dex for FGK stars respectively. In deriving Eq. 20 as a function of spectral type, Santos et al. (2000) computed spectral types for each star in their sample based on their CORALIE spectra. However we lack such spectra and instead define the boundaries between FGK stars based on T_{eff} given the limited information available for the TOIs. The assumed ranges are $T_{\text{eff,F}} \in (6000, 7500]$ K, $T_{\text{eff,G}} \in (5200, 6000]$ K, and $T_{\text{eff,K}} \in (3800, 5200]$ K. By computing $\log R'_{\text{HK}}$ and its uncertainty from sampled values of P_{rot} and $B - V$, we can map from $\log R'_{\text{HK}}$ to the distribution of σ_{act} for the active FGK stars in the sample of planet-hosting TOIs.

Lastly, for M dwarfs there exists a clean relation between $\log R'_{\text{HK}}$ and P_{rot} (Astudillo-Defru et al. 2017a). The correlation saturates at a maximum mean value of $\log R'_{\text{HK}} = -4.045$ for rapid rotators with $P_{\text{rot}} < 10$ days and falls off with rotation period out to the slowest rotating observed M dwarfs with $P_{\text{rot}} \gtrsim 100$ days. Explicitly, Astudillo-Defru et al. (2017a) find the best-fit step-wise powerlaw to the correlation:

$$\log R'_{\text{HK}} = \begin{cases} -1.509 \log P_{\text{rot}} - 2.550, & P_{\text{rot}} > 10 \text{ days} \\ -4.045, & P_{\text{rot}} \leq 10 \text{ days.} \end{cases} \quad (21)$$

The dispersion in the relation for slow rotators is characterized by the uncertainty in the slope and intercept of 0.007 and 0.020 respectively whereas the dispersion in $\log R'_{\text{HK}}$ for rapid rotators is 0.093. Sampled values of P_{rot} for M dwarfs are used to map to $\log R'_{\text{HK}}$ using Eq. 21 from which σ_{act} values are estimated using a relation similar to Eq. 20 but extrapolated to M dwarfs with

$T_{\text{eff}} \leq 3800$ K. The adopted coefficient and powerlaw index for M dwarfs (2 m s^{-1} and 0.1 respectively) were derived from the set of 23 M dwarfs with $2 \lesssim P_{\text{rot}} \lesssim 150$ days (c.f. Fig. 3 Cloutier et al. 2018) whose RV activity rms was characterized with HARPS (X. Delfosse private communication). Additional empirical data to further calibrate these models for M dwarfs are part of an on-going study with HARPS (Delfosse et al. in prep.) and with a subset of active M dwarfs from CARMENES recently reported (Tal-Or et al. 2018).

We note that the empirical distributions of RV activity used in this study were derived from observations using optical spectrographs. However, RV activity signals are known to be chromatic as they largely depend on the temperature contrast between an active region and the stellar photosphere where the contrast effect is known to decrease from the optical to the near-IR (e.g. Martín et al. 2006; Huélamo et al. 2008; Prato et al. 2008; Reiners et al. 2010; Mahmud et al. 2011). Meanwhile, Zeeman broadening of spectral features increases with wavelength (Reiners et al. 2013). The dominant source for RV activity as a function of wavelength and spectral type is not yet fully understood (Moutou et al. 2017) and so we choose to remain agnostic and set the near-IR RV activity equal to that which is derived in the optical.

2.5. Estimating RV noise due to unseen planets

The occurrence rates of planets of various sizes around FGKM stars was well studied with the primary *Kepler* mission (e.g. Fressin et al. 2013; Dressing & Charbonneau 2015). For example, the cumulative occurrence rate of planets with radii $r_p \in [0.8, 22] R_{\oplus}$ around FGK stars out to 418 days is $\gtrsim 0.87$ planets (Fressin et al. 2013). For M dwarfs, small planets with $r_p \in [0.5, 4] R_{\oplus}$ with $P \leq 200$ days appear to be more common with at least 2.5 such planets per M dwarf. In the TESS simulations of S15 up to one transiting planet is detected although the multiplicity of each simulated planetary system is reported. Here we use the number of additional planets around each TOI—along with the known occurrence rates of planets—to estimate the RV contribution due to these planets whose transits are not characterized with TESS.

For TOIs with a reported multiplicity $N_p > 1$, we sample the radius r_p and orbital period P of the $N_p - 1$ additional planets from the *Kepler*-derived occurrence rates from Fressin et al. (2013) for FGK dwarfs or from Dressing & Charbonneau (2015) for M dwarfs. Because at most only one planet is detected in transit for each TOI and the transit probability $\propto P^{-2/3}$, we draw the orbital periods of additional planets from values greater than the reported orbital period of the known TESS planet. In this way the TESS planet is always the innermost planet in the system and therefore most likely to transit. However, inner non-transiting planets have been detected in known transiting systems as a result of a potentially small mutual inclination ($\Delta i \sim 1^\circ$; Cloutier et al. 2017b).

When sampling the planet occurrence rates as a function of P and r_p , $f(P, r_p)$, a few caveats arise. Firstly, $f(P, r_p)$ are reported over a coarse grid. Therefore when drawing a planet with a range of potential orbital periods and radii we sample the exact value of P and r_p each from a uniform distribution bounded by the edges of that bin. Secondly, due to the poor detection sen-

sitivity to the smallest planets at large orbital periods, $f(P, r_p)$ is poorly constrained there. To quantify the values of $f(P, r_p)$ in this regime we assume that $f(P, r_p)$ evolves smoothly such that in bins where $f(P, r_p)$ is poorly constrained, we can average the measured values in surrounding bins to populate the previously vacant bin. We restrict all pairs of planets in multi-planet systems to remain Lagrange stable according to the analytic condition from Barnes & Greenberg (2006) while assuming circular orbits for all planets. Lastly, the sampled radii for all additional planets are converted to a planetary mass m_p according to the empirically derived mean mass-radius relations from Weiss et al. (2013) or Weiss & Marcy (2014),

$$\frac{m_p}{M_{\oplus}} = \begin{cases} 0.440 \left(\frac{r_p}{R_{\oplus}}\right)^3 + 0.614 \left(\frac{r_p}{R_{\oplus}}\right)^4, & r_p < 1.5 R_{\oplus} \\ 2.69 \left(\frac{r_p}{R_{\oplus}}\right)^{0.93}, & 1.5 \leq r_p/R_{\oplus} < 4 \\ \left(0.56 \left(\frac{r_p}{R_{\oplus}}\right) \left(\frac{S}{336.5S_{\oplus}}\right)^{0.03}\right)^{1.89}, & 4 \leq r_p/R_{\oplus} < 13.7 \\ \mathcal{U}(150, 2000), & r_p \geq 13.7 R_{\oplus} \end{cases} \quad (22)$$

where S is the irradiance received by the planet. By adopting the mean mass-radius relation this formalism neglects to reflect the diversity of exoplanet masses for a given planet radius.

The sinusoidal keplerian solution with unit amplitude has an rms value of $\sqrt{2}/2 \sim 0.707$. Therefore for each additional planet $i = 1, \dots, N_p - 1$, we can calculate $\sigma_{\text{planets}, i} = 0.707 K_i$ where K_i is the planet's semi-amplitude computed from its sampled P_i , $m_{p, i}$, and host stellar mass. The total value of σ_{planets} is calculated by the quadrature addition of $\sigma_{\text{planets}, i}$ from each additional planet whose $K_i > \sigma_{\text{RV}}$. This latest condition is imposed assuming that additional planets not seen in-transit but whose semi-amplitudes are large compared to the RV measurement precision will be accurately modelled in the RV analysis and therefore not contribute to the residual RV rms.

2.6. Exposure time calculator

Together with estimates of N_{RV} , the exposure time t_{exp} per TOI can be used to calculate the total observing time required to detect a TESS planet in radial velocity. For a given star, the exposure time required to achieve a desired S/N per resolution element will depend on the properties of the spectrograph and telescope used as well as on the star's magnitude in the spectral bands spanned by the spectrograph. For each TOI in this study we calculate the exposure time that is required to reach a S/N of at least 100 at the center of a reference band; V ($\lambda = 0.55 \mu\text{m}$) or J ($\lambda = 1.25 \mu\text{m}$) for optical and near-IR spectrographs respectively. The zero point flux densities in each spectral band used to calculate the S/N = $\sqrt{N_e}$ per resolution element are reported in Table 1.

The benefit of integrating longer is only to achieve a photon-noise limited RV precision less than a few σ_{act} , is one of diminishing returns because the effective RV precision becomes dominated by activity and cannot be reduced by increasing t_{exp} . Although, it is important to note that increasing t_{exp} permits a better sampling for

the spectral CCF thus improving one’s ability to accurately characterize the activity and mitigate its effects. In cases for which the calculated t_{exp} results in $\sigma_{\text{RV}} > \sigma_{\text{act}}$ or $>$ the expected K , we claim that the exposure time is under-estimated. To remedy this we scale-up t_{exp} to achieve $\sigma_{\text{RV}} \lesssim \sigma_{\text{act}}$ and \lesssim the expected K . In our exposure time calculator we do impose restrictions on the range of t_{exp} that can be considered. Specifically, we restrict $t_{\text{exp}} \in [10, 60]$ minutes. The shortest permissible exposure time is required to help mitigate the effects of stellar pulsations and surface granulation which evolve on timescales $\lesssim 10$ minutes (Lovis et al. 2005; Dumusque et al. 2011). The upper limit of 60 minutes is applied in order to limit the total observing time dedicated to a single star. In practice, the majority of stars requiring > 60 minutes to achieve the target S/N per resolution element and beat the RV activity rms, will result in a correspondingly low σ_K and will therefore not be amenable to RV characterization within a reasonable timespan. We do note that this upper limit is chosen somewhat arbitrarily and some observers may wish to increase the maximum exposure time to accommodate certain high-value targets such as temperate Earth-like planets within or near their host star’s habitable zone⁸.

3. MODEL COMPARISON TO OBSERVATIONS

In Sect. 2 we derived Eq. 18 for the number of RV observations required to measure K of a transiting planet with a precision of σ_K in an RV time-series with white noise and an effective RV uncertainty σ_{eff} . Similar calculations can be made of $\sigma_K(N_{\text{RV}})$ in the presence of correlated noise using the formalism discussed in Sect. 2.1.2 and Eq. 13. Here we compare our analytic estimates of N_{RV} —under the applicable noise condition—to observational results from existing RV time-series to ensure that our model provides an accurate approximation to N_{RV} when applied to the TOIs. We consider two sets of RV time-series of transiting planetary systems featuring either a white or correlated noise model. The latter models being restricted to a quasi-periodic GP treatment of correlated RV residuals as was assumed in Sect. 2.1.2. All systems considered must also obey the assumptions imposed when deriving σ_K . To recapitulate, those assumptions are:

1. the planet’s orbital solution is well-approximated as circular.
2. The value of the TESS planet’s P and T_0 are known to ultra-high precision compared to K such that correlations between the measured values of P , T_0 , and K are unimportant.
3. The window function of the RV time-series is (approximately) sampled uniformly over the planet’s full orbital phase.
4. The white RV time-series have a characteristic scalar RV uncertainty equal to the rms of the RV residuals.

⁸ There are approximately nine temperate Earth-like planets that will be discovered with TESS with $T_{\text{eq}} \in [185, 300]$ K and $r_p \leq 1.5 R_{\oplus}$ (S15).

TABLE 2
SUMMARY OF RV OBSERVATIONS FOR KNOWN TRANSITING PLANETS WITH WHITE RV NOISE

Planetary System	σ_{eff} [m s ⁻¹]	σ_K [m s ⁻¹]	Actual N_{RV}	Calculated N_{RV}	Ref.
GJ 1132	3.38	0.92	25	27.0	1
GJ 1214	4.96	1.60	21	19.2	2
HAT-P-4	10.20	3.00	23	23.1	3
HAT-P-8	10.23	4.20	16	11.9	3
HAT-P-10	6.56	2.70	13	11.8	3
HAT-P-12	5.05	1.60	23	19.9	3
HAT-P-18	20.30	5.20	31	30.5	3
HAT-P-22	9.70	3.20	18	18.4	3
HAT-P-24	13.00	3.60	24	26.1	3
HAT-P-26	3.60	0.98	26	27.0	3
HAT-P-29	11.20	4.60	11	11.9	3
HAT-P-33	66.00	17.50	26	28.4	3
HD 97658	2.78	0.39	96	101.6	4
HD 149026	6.18	1.40	42	39.0	3
HD 189733	15.00	6.00	12	12.5	5
HIP 116454	2.01	0.50	33	32.3	6
Kepler-10	3.55	0.34	220	218.0	7
Kepler-78	2.60	0.40	79	84.5	8
Kepler-93 ^a	1.86	0.27	86	94.9	9
TrES-2	18.10	5.70	19	20.2	3
TrES-4	16.90	10.00	6	5.7	3
WASP-1	7.00	3.20	10	9.6	3
WASP-3	17.60	5.90	15	17.8	3
WASP-4	3.25	2.30	5	4.0	3
WASP-16	2.62	1.60	4	5.36	3
WASP-18	8.77	6.20	6	4.0	3
WASP-19	20.35	5.00	34	33.1	3
WASP-24	4.62	3.20	4	4.2	3
WASP-34	3.60	1.70	8	9.0	3
XO-2N	19.00	8.00	10	11.3	10
XO-5	11.20	3.00	24	27.9	3

NOTE. — **References:** (1) Berta-Thompson et al. (2015), (2) Charbonneau et al. (2009), (3) Knutson et al. (2014), (4) Howard et al. (2011), (5) Bouchy et al. (2005), (6) Vanderburg et al. (2015), (7) Weiss et al. (2016), (8) Howard et al. (2013), (9) Dressing et al. (2015), (10) Burke et al. (2007)

^a HARPS-N measurements only.

To make the analytic estimates of N_{RV} for each observed planetary system featuring a white noise model, we use the 1σ value of σ_K for one planet in the system. By the nature of the Fisher information the value of σ_K for each modelled planet in a multi-planet system should be equal so long as all ephemerides are well-constrained and planet semi-amplitudes are not correlated. Indeed, the measured planet semi-amplitudes should be uncorrelated when all planets’ are weakly interacting with distinct orbital periods. For each RV time-series we set the value of σ_{eff} to the rms of the RV residuals following the removal of all RV signals modelled by the authors. Some authors report their residual rms values explicitly whilst others treat the stellar activity signal as white by fitting an additive scalar jitter parameter that we add in quadrature to the median RV measurement uncertainty of the time-series to estimate σ_{eff} . The planetary systems with white noise models considered in this analysis are summarized in Table 2.

To compare our formalism in the presence of correlated noise to observed systems we consider five cases analyzed with a quasi-periodic GP correlated noise activity model. Namely CoRoT-7 (Haywood et al. 2014), K2-18 (Cloutier et al. 2017b), Kepler-21 (López-Morales et al. 2016), Kepler-78 (Grunblatt et al. 2015), and LHS 1140 (Dittmann et al. 2017). The calculated value of N_{RV} for these systems is obtained by evaluating σ_K from

Eq. 13 using each systems’ unique RV time-series \mathbf{t} , \mathbf{y} , and σ_{RV} from their respective papers along with the semi-amplitude and GP hyperparameter values plus uncertainties. The maximum likelihood parameter values are reported in Table 3. Because the model parameters are known to a finite precision we Monte-Carlo sample each model parameter from a Gaussian distribution whose mean is equal to its best-fit value and standard deviation equal to the parameter’s measured 1σ uncertainty. Evaluating the Fisher information matrix with 10^3 model parameter draws results in a distribution of σ_K for each planet from which the distribution of N_{RV} can be calculated using Eq. 18 after σ_{eff} is derived identically to as in the white noise scenario.

Analytic estimates of N_{RV} are compared to observed values for known planetary systems in Fig. 1. As evidenced in Fig. 1, the majority of planetary systems have calculated N_{RV} values in close agreement with observed values for both the white and correlated noise scenarios. This demonstrates that our analytical models for N_{RV} are valid for the majority of cases with one notable exception. Quantitatively, the rms of the O-C N_{RV} values is 2.6 for the white noise cases alone and 5.2 for all planetary systems included in Fig. 1 with the exception of the curious outlier LHS 1140. Our calculated value of N_{RV} for LHS 1140 is overestimated relative to the size of the RV time-series presented in Dittmann et al. (2017) from which K is measured to be $5.34 \pm 1.1 \text{ m s}^{-1}$. After Monte-Carlo sampling K and the GP hyperparameters from their measurement uncertainties we calculate a median $N_{RV} = 265 \pm 64$ which is ~ 1.8 times greater than the actual time-series size ($N_{RV} = 144$) at 1.9σ . The exact cause of this anomalous discrepancy is not known but may be related to how the GP covariance function is implemented although this investigation is beyond the scope of this paper.

4. OVERVIEW OF COMPUTING N_{RV} FOR THE EXPECTED TESS PLANET POPULATION

S15 predicted the population of planets that will be discovered with TESS in its 2-minute cadence observing mode. Their results are provided for one realization of their simulations and contains 1984 TOIs, each with a single transiting planet. The properties of their stellar sample is copied in Table 6 for easy reference. This realization contains more detected planets than the average of their simulations; ~ 1700 . We treat each TOI in the S15 sample as a bona-fide exoplanet and not as a false positive. However, some number of TOIs will ultimately be identified as false positives as historically the false positive rate of transit surveys like Kepler have yielded higher false positive rates than initially anticipated (Sliski & Kipping 2014; Morton et al. 2016). The properties of the adopted planet population were derived from planet occurrence rates measured with Kepler circa 2015. Some planetary properties, particularly the planetary radii, have since been modified slightly following the reanalysis of Kepler-planet host star properties (e.g. Fulton et al. 2017).

Here we compute analytical estimates of N_{RV} required to measure a planet’s RV semi-amplitude—at a given precision—for the entire synthetic catalog of TESS planets from S15. Together with the exposure time calculator described in Sect. 2.6 we calculate the total observing

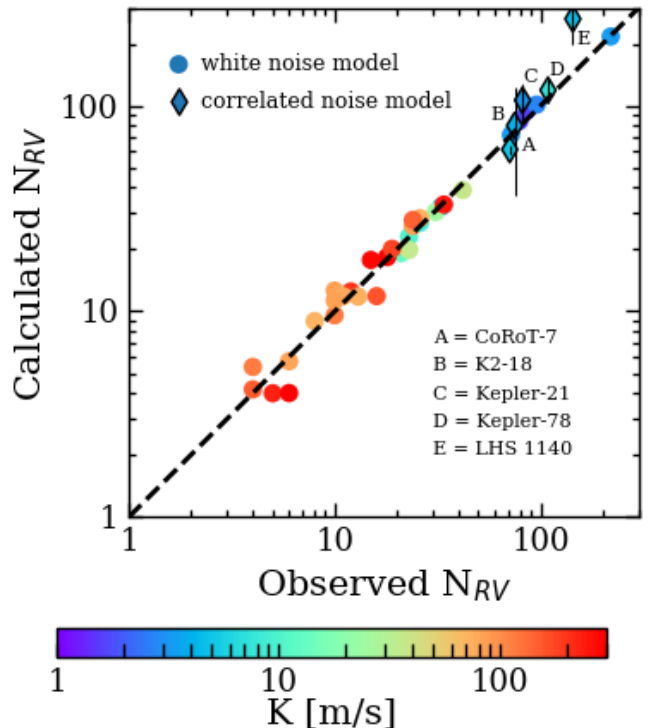


FIG. 1.— Observed values of N_{RV} compared to the calculated values including either white or correlated RV noise for a suite of known transiting planetary systems. The colorbar indicates each planet’s RV semi-amplitude. The dashed line depicts the line $y = x$ wherein calculated N_{RV} correspond exactly to the observed N_{RV} . The region above the line depicts where the observed N_{RV} —for a given K measurement precision—are less than the value predicted by the Fisher information and would be considered anomalous. The region below the line depicts where the observed N_{RV} are larger than the value predicted by the Fisher information implying that the K measurement uncertainty may be under-estimated.

time required to detect each planet. These calculations require estimates of RV noise sources from the RV noise floor of the employed spectrograph, photon noise, activity, and additional unseen planets. Photon noise is dependent on the RV information content contained within the stellar spectrum and varies across spectral bands. Therefore we consider RV follow-up observations taken with either a fiducial optical spectrograph or a fiducial near-IR spectrograph. The specifications corresponding to our adopted optical spectrograph are modelled after the HARPS spectrograph on the 3.6m ESO telescope at La Silla observatory (Mayor et al. 2003). The specifications corresponding to our adopted near-IR spectrograph are modelled after the up-coming NIRPS spectrograph that will join HARPS at the 3.6m ESO telescope at La Silla observatory in 2019 (Bouchy et al. 2017). The adopted specifications for our two fiducial spectrographs are given in Table 4. Using the formalism discussed in Sect. 2.2 we calculate σ_{RV} for each TOI with both spectrographs. For reference, the distributions of TOI σ_{RV} for both spectrographs are shown in Fig. 2.

In Sect. A we will present a web-based $N_{RV}(\sigma_{RV})$ calculator that can be used to repeat these calculations but using any spectrograph defined by the user.

As discussed in Sects. 2.3, 2.4, and 2.5, estimates of N_{RV} are also sensitive to additive RV noise sources such as stellar activity and unseen planets. However, these astrophysical noise sources are not known a-priori for the

TABLE 3
SUMMARY OF RV OBSERVATIONS FOR KNOWN TRANSITING PLANETS WITH RED RV NOISE

Planetary System	K [m s ⁻¹]	a [m s ⁻¹]	λ [days]	Γ	P_{GP} [days]	σ_{jitter} [m s ⁻¹]	σ_{eff} [m s ⁻¹]	σ_K [m s ⁻¹]	Actual N_{RV}	Median Calculated N_{RV}	Ref.
CoRoT-7	3.42	7.0	20.6	1.0	23.8	3.44	3.93	0.66	71	61.4 ± 2.7	1
K2-18	3.18	2.8	59.1	1.2	38.6	0.25	4.59	0.75	75	80.3 ± 43.7	2
Kepler-21	2.12	6.7	17.0	2.4	12.6	1.98	4.22	0.66	82	106.7 ± 20.8	3
Kepler-78	1.86	5.6	18.5	2.5	13.3	1.10	1.85	0.25	109	119.4 ± 15.0	4
LHS 1140	5.3	9.0	277.9	2.0	134.0	3.0	9.33	1.1	144	265.5 ± 64.4	5

NOTE. — **References:** (1) Haywood et al. (2014), (2) Cloutier et al. (2017b), (3) López-Morales et al. (2016), (4) Grunblatt et al. (2015), (5) Dittmann et al. (2017)

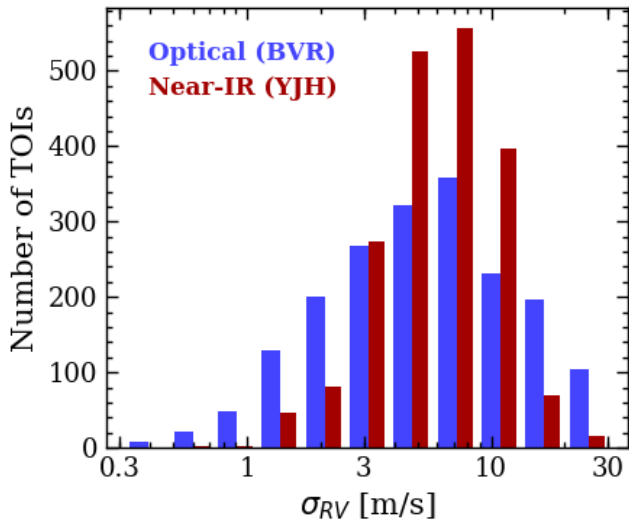


FIG. 2.— The distributions of the TOI photon-noise limited RV measurement precisions derived from PHOENIX stellar models and using the formalism discussed in Sect. 2.2. The values of σ_{RV} are computed for each of our fiducial spectrographs in the optical and near-IR with spectral bands *BVR* and *YJH* respectively (see Table 4).

TABLE 4
FIDUCIAL SPECTROGRAPH SPECIFICATIONS

	Optical	Near-IR
Spectral bands	<i>BVR</i>	<i>YJH</i>
Spectral resolution, R	115,000	100,000 ^a
Telescope aperture, D [m]	3.6	3.6
RV noise floor, σ_{floor} [m s ⁻¹]	0.5	1.0
Throughput, ϵ	0.05	0.05

^a We consider the higher resolution achievable in the NIRPS High Accuracy Mode relative to its High Efficiency Mode at $R = 75,000$.

S15 TOIs and therefore must be sampled from known distributions of applicable values of σ_{act} and σ_{planets} . A Monte-Carlo sampling routine is used for each TOI to sample the aforementioned quantities from the distributions discussed in Sects. 2.4 and 2.5. The value of N_{RV} for each TOI also depends on the desired K measurement uncertainty that is set by the nature of the follow-up science that one wishes to conduct once the planet’s mass has been characterized with RVs. For example, conventionally the *detection* of a planet’s K requires a 3σ detection significance; $3 = K/\sigma_K$. Conversely, targets that will be amenable to atmospheric characterization via transmission spectroscopy will benefit from a more

precise measurement of the planet’s bulk density that in-turn requires a mass detection significance $> 3\sigma$.

In the following Sect. 5 we present results of N_{RV} for the full TESS sample in the limit of correlated RV noise (see Sect. 2.1.2). We also consider four subsamples of TESS planets each pertaining to a unique science case that will be addressed by TESS. Each science case merits a unique choice of σ_K for a particular subset of TOIs. Total observing times are then calculated as $N_{\text{RV}} \cdot (t_{\text{exp}} + t_{\text{overhead}})$. Because the exact value of t_{overhead} varies between observatories, we will set $t_{\text{overhead}} = 0$ such that its effect can easily be added to the total observing times later-on for non-zero values. To estimate N_{RV} in the presence of correlated RV noise we construct time-series of increasing N_{RV} from $10 - 10^3$ in steps of 90. For our time-series we adopt a simple uniform window function \mathbf{t} spanning 100 days which is sufficient to sample the full orbit of $\sim 99\%$ of TOIs. Such simplistic time sampling is admittedly unrealistic given the expected number and frequency of nights lost due to poor observing conditions (clouds, poor seeing, etc). To that end we tested more complex window functions which included longer baselines and gaps due to observing seasons. We found results roughly consistent with the uniform window functions although this need not be true for *any* window function with arbitrary complexity such as those which are often obtained in practice over many observing seasons. For each of the 12 time-series with a unique N_{RV} we compute σ_K before interpolating $N_{\text{RV}}(\sigma_K)$ to the desired value of σ_K . The initial guesses of the GP hyperparameters $\{\lambda, \Gamma, P_{\text{GP}}\}$ are adopted from from Dittmann et al. (2017) (see Methods section *Radial-velocity analysis with Gaussian process regression.*) with the remaining GP hyperparameters set to $a = \sqrt{2}\sigma_{\text{act}}$ and $\sigma_{\text{jitter}} = \sigma_{\text{planets}}$. The RV time-series $\mathbf{y}(\mathbf{t})$ contains keplerian contribution from the TESS planet and other sampled planets if applicable, plus correlated noise from a sample of the GP prior distribution, and white noise featuring contributions from the RV noise floor of the spectrograph (Table 4) and the photon-noise limited measurement precision: $\sqrt{\sigma_{\text{floor}}^2 + \sigma_{\text{RV}}^2}$. The RV measurement uncertainty time-series $\sigma_{\text{RV}}(\mathbf{t})$ contains the aforementioned value repeated N_{RV} times.

5. RESULTS FOR THE TESS SAMPLE

5.1. Detecting all TESS planet masses at 3σ

Here we present the results of attempting to detect the masses of *all* TESS planets at 3σ using either the optical or near-IR spectrograph. As such, we do not make a cut in declination and restrict targets to half of the sky. Our fiducial spectrographs are intended to be representa-

tive of suites of spectrographs—with comparable on-sky performance—thus providing full sky coverage. Realistically not all TESS planets will be characterized with RVs due to either their small RV semi-amplitude, certain intrinsic stellar host properties that deter RV observations (e.g. a low apparent magnitude, rapid projected stellar rotation, or high levels of stellar activity), or simply due to a lack of available observing time. Despite this fact we present the results for *all* TESS planets.

Detecting a planet’s mass at 3σ requires a K detection significance that is slightly larger than three because the calculation of m_p from K is also dependent on other observables such as the orbital period and stellar mass whose measurement uncertainties contribute to the m_p measurement uncertainty. To calculate the value of σ_K required to achieve $m_p/\sigma_{m_p} = 3$ we first assume that the orbital period of the planet is known to a sufficiently high fractional precision relative to the other parameters of interest (i.e. $\sigma_P/P \ll 1$) such that its contribution to σ_{m_p} can be effectively ignored. Secondly, we assume throughout this study that all stellar masses are measured with a conservative precision of 10% as many field dwarfs in the solar neighbourhood have their masses measured with a precision of $\lesssim 10\%$ from mass-luminosity relations (Delfosse et al. 2000; Torres et al. 2010). However, this assumed fractional precision will not hold for all TOIs as a subset will have their masses characterized more precisely using other advanced techniques such as asteroseismology or spectroscopy coupled with precision parallaxes (e.g. Van Eylen et al. 2017; Fulton & Petigura 2018). We note that the calculations presented here represent conservative values if TOI stellar masses can be determined to a precision higher than 10%. Nevertheless, under our current assumptions a 3.06σ detection of K (i.e. $\sigma_K = 0.327K$) is required to detect m_p at 3σ .

The median results—over Monte-Carlo realizations—of our calculations are reported in Table 7 for each TOI. Specifically, we report the median photon noise-limited RV precision in both the optical and near-IR spectrographs, σ_{act} , σ_{planets} , N_{RV} , and total observing times in each spectrograph; $t_{\text{obs,opt}}$ and $t_{\text{obs,nIR}}$. The values of N_{RV} —and the corresponding t_{obs} —are derived from the general case which includes a GP treatment of correlated RV noise.

In Fig. 3 we compare $t_{\text{obs,opt}}$ and $t_{\text{obs,nIR}}$ as a function of TOI effective temperature to ascertain which flavor of spectrograph is favorable for efficient RV planet mass characterization. A clear trend is discernible with the ratio of the median optical to the near-IR total observing times decreasing towards earlier spectral types. Efficient characterization of planets around late TOIs with $T_{\text{eff}} \lesssim 3800$ K is significantly favoured by the use of near-IR spectrographs due to the reduced photon noise exhibited by those stars in the near-IR. Conversely for TOIs with $T_{\text{eff}} \gtrsim 5500$ K, the optical spectrograph is preferred. For intermediate TOIs the two spectrographs offer nearly consistent performance.

Modulo the effects of rotation and stellar activity the observing time required to detect a transiting planet with RVs is dependent on the host star’s brightness and spectral type which directly effect σ_{RV} . Recall that our derived values of σ_{RV} for each TOI are based on stellar spectral models rather than on empirical spectra such as the M dwarfs observed at high resolution ($R > 80,000$) with

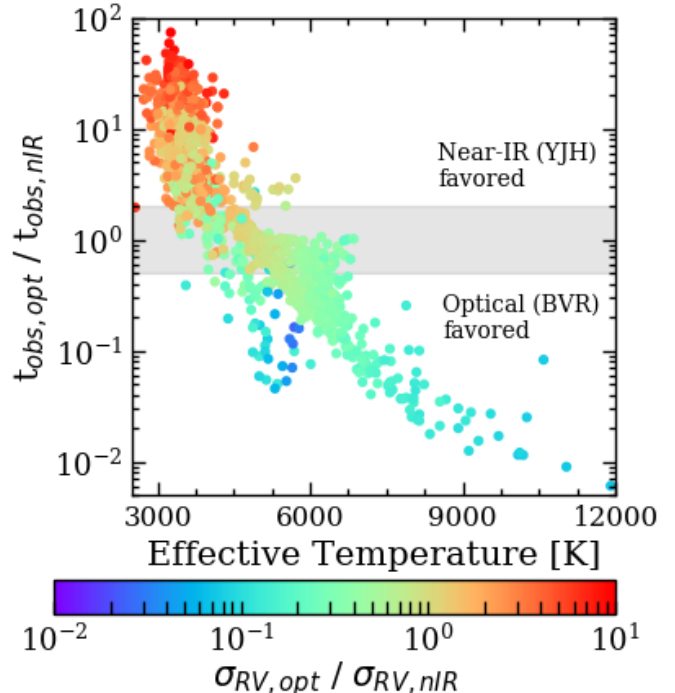


FIG. 3.— Point estimates of the ratio of the median total observing times with an optical spectrograph to with a near-IR spectrograph as a function of TOI effective temperature. Colors are indicative of the ratio of the photon-noise limited RV precision in the optical to the near-IR. Near-IR RV observations are a more efficient means of planet mass characterization when this ratio is a few times unity. Conversely, optical RV observations are a more efficient means of planet mass characterization when this ratio is a few times smaller than unity. The shaded region spanning the ordinate $\in [1/2, 2]$ approximately depicts where the use of either an optical or near-IR spectrograph offer nearly consistent performance.

the CARMENES visible and near-IR channels (Reiners et al. 2017). Reiners et al. (2017) claim that the RV information content peaks in the RI bands between 700-900 nm for all M dwarfs. This empirical evidence somewhat contradicts theoretical calculations based on model spectra (e.g. Figueira et al. 2016, this study), especially for late M dwarfs whose RV information content is theorized to peak in the HK bands from 1.4-2.4 μm . Convergence towards a more precise scaling of σ_{RV} with wavelength—for stars of various spectral types—will be achieved in the near future with the onset of multiple new spectrographs from the optical to the near-IR.

5.1.1. Detecting TESS planet masses versus TOI spectral type

The cumulative median observing time required to detect TESS planets as a function of TOI spectral type is shown in Fig. 4 up to 10^3 hours. The results are also given in terms of the cumulative number of observing nights assuming a notional value of 7 observing hours per night. We consider spectral type bins with the following adopted definitions: mid-late M dwarfs: $2500 \leq T_{\text{eff}}/K < 3200$, early-mid M dwarfs: $3200 \leq T_{\text{eff}}/K < 3800$, FGK dwarfs: $3800 \leq T_{\text{eff}}/K < 7600$, and BA dwarfs: $7600 \leq T_{\text{eff}}/K < 12000$. Spectral type bins are considered separately because of the clear trend exhibited in total observing times with either an optical or near-IR spectrograph with T_{eff} as seen in Fig. 3. For example, it is clear that all 39 TESS planets around BA

stars can be detected with our optical spectrograph in ~ 140 nights whereas only ~ 12 of those planets can be detected with the near-IR spectrograph in a thousand hours (i.e. ~ 143 nights). Planet detections around Sun-like stars (i.e. FGK) are obtained more efficiently with the optical spectrograph with $\sim 251/964$ optical detections compared to $\sim 198/964$ near-IR detections in a thousand hours. Efficient M dwarf planet detections favor the near-IR spectrograph wherein a thousand hours of observing time yields $\sim 165/927$ early-mid M dwarf planets or nearly all ~ 54 mid-late M dwarf planets. These numbers are reduced to $\sim 60/927$ and $\sim 21/54$ in a thousand hours with our optical spectrograph.

Further demonstrated in Fig. 4 is the first derivative of the total number of planet detections with cumulative observing time; dN/dt . This quantity describes the efficiency of detecting planets over time as large values of the derivative highlight when planet masses may be detected in a short amount of observing time. We will continue by referring to this quantity as the *detection efficiency*. The detection efficiency can be used to identify after how much total observing time further planet detections become too observationally expensive. That is that when the detection efficiency drops below a set threshold value, any additional planet detections will require too much observing time that may otherwise be spent on potentially more feasible targets. For reference in Fig. 4 we highlight the value of the inverse time derivative—which is still a measure of detection efficiency—equal to 20 hours per detection. We suggest this value as a minimum derivative value. With this threshold value planets around BA stars should be observed for up to ~ 29 nights with an optical spectrograph before the detection efficiency drops below this threshold value. Similarly, planets around mid-late M dwarf TOIs should be observed for ~ 43 nights with a near-IR spectrograph. Observing Sun-like and early-mid M dwarf stars can mostly proceed efficiently beyond 10^3 hours when using either spectrograph however observing early-mid M dwarfs slowly approaches 20 hours per detection after ~ 110 nights. Observing all TOIs with the optical spectrograph—or with a network of optical spectrographs of comparable performance—until we reach a detection efficiency of 20 hours per detection would require ~ 800 nights of cumulative observing time. In that time, ~ 620 planets could be detected around TOIs of any spectral type with $V \leq 15$. Repeating this observing campaign with the near-IR spectrograph—or with a network of near-IR spectrographs of comparable performance—would require ~ 1600 nights of cumulative observing time. In that time ~ 1030 planets could be detected around TOIs of any spectral type with $J \leq 13.6$.

5.1.2. Detecting TESS planet masses versus planet type

The cumulative median observing times required to detect TESS planets as a function of planet type are shown in Fig. 5 up to 10^3 hours. We consider four types of planet defined by their radii to be Earths ($< 1.25 R_{\oplus}$), super-Earths ($1.25 - 2 R_{\oplus}$), Neptunes ($2 - 4 R_{\oplus}$), and giants ($> 4 R_{\oplus}$).

Of the 1984 planets in the S15 TESS sample, 66 are classified as Earths with 26 around stars with $V \leq \text{median}(V) = 13.5$ and 36 around stars with $J \leq \text{median}(J) = 10.7$. Most Earths will be detected in-

transit around M dwarfs ($T_{\text{eff}} \leq 3800$ K) due to their favorable transit depths. With a thousand hours of total observing time we expect $\sim 26/66$ Earths to be detected with the near-IR spectrograph compared to ~ 15 detections in the optical. We note that detections of the smallest planets can be expensive as the detection efficiency exceeds 20 hours per detection after ~ 11 nights or after just ~ 8 detections in the near-IR. The detection efficiency drops more rapidly in the optical to greater than 20 hours per detection after just ~ 6 nights or ~ 4 detections.

Super-Earths can be detected rather efficiently in the near-IR to beyond 10^3 hours and with an optical detection efficiency better than 20 hours per detection up to ~ 100 nights. We expect to yield $\sim 100/509$ super-Earths with either the optical or near-IR spectrographs after 10^3 observing hours. Neptunes are the most efficiently detected class of planet and with similar detection efficiencies between the two spectrographs. $\sim 220/1258$ Neptune detections are expected in a thousand hours in the optical compared to $\sim 180/1258$ in the near-IR. For Neptunes the detection efficiency remains < 20 hours per detection for up to after ~ 510 nights or ~ 370 detections in the optical and after ~ 960 nights or ~ 660 detections in the near-IR. Lastly, $\sim 130/151$ giant planets are detected in the optical in ~ 80 nights at which point the optical detection efficiency begins to exceed 20 hours per detection. Similarly in the near-IR, $\sim 110/151$ giant planets are detected in ~ 85 nights.

5.2. Science Case 1: mass characterization of 50 TESS planets with $r_p < 4 R_{\oplus}$

The TESS level one science requirement is to measure the masses of 50 small transiting planets with $r_p < 4$ Earth radii.⁹ To date, the vast majority of masses for planets with $r_p < 4 R_{\oplus}$ have been obtained with HARPS, HARPS-N, and HIRES. The onset of many up-coming precision velocimeters will provide many more instruments capable of characterizing such planets. Similarly to Sect. 5.1, we define a planet mass measurement requirement for the completion of the TESS level one science requirement of 5σ . Given our previous assumptions regarding the measurement precision on P and M_s (see Sect. 5.1), a 5σ mass detection requires a $5.29\sigma K$ detection (i.e. $\sigma_K = 0.189K$). According to our analytic model for N_{RV} in the white noise limit, a 5σ mass detection requires $(0.327/0.189)^2 = 2.99$ more observing time than a 3σ mass detection.

The cumulative median observing time required to complete the TESS level one science requirement is shown in Fig. 6. Here we calculate the cumulative median observing times from various planet samples: i) the 50 small TESS planets sorted in ascending order by total observing times (i.e. the most efficient characterization of 50 small planet masses possible) and ii) for random subsets of the small TESS planets. The latter cases correspond to attempting to conduct RV follow-up observations of *any* subset of small TESS planet up to 50 such planets. In total there are 1833 TESS planets with $r_p < 4 R_{\oplus}$ which causes the cumulative observing time to vary drastically depending on whether the input planet set is sorted or random. This is evidenced in Fig. 6 wherein it is

⁹ <https://tess.mit.edu/followup/>

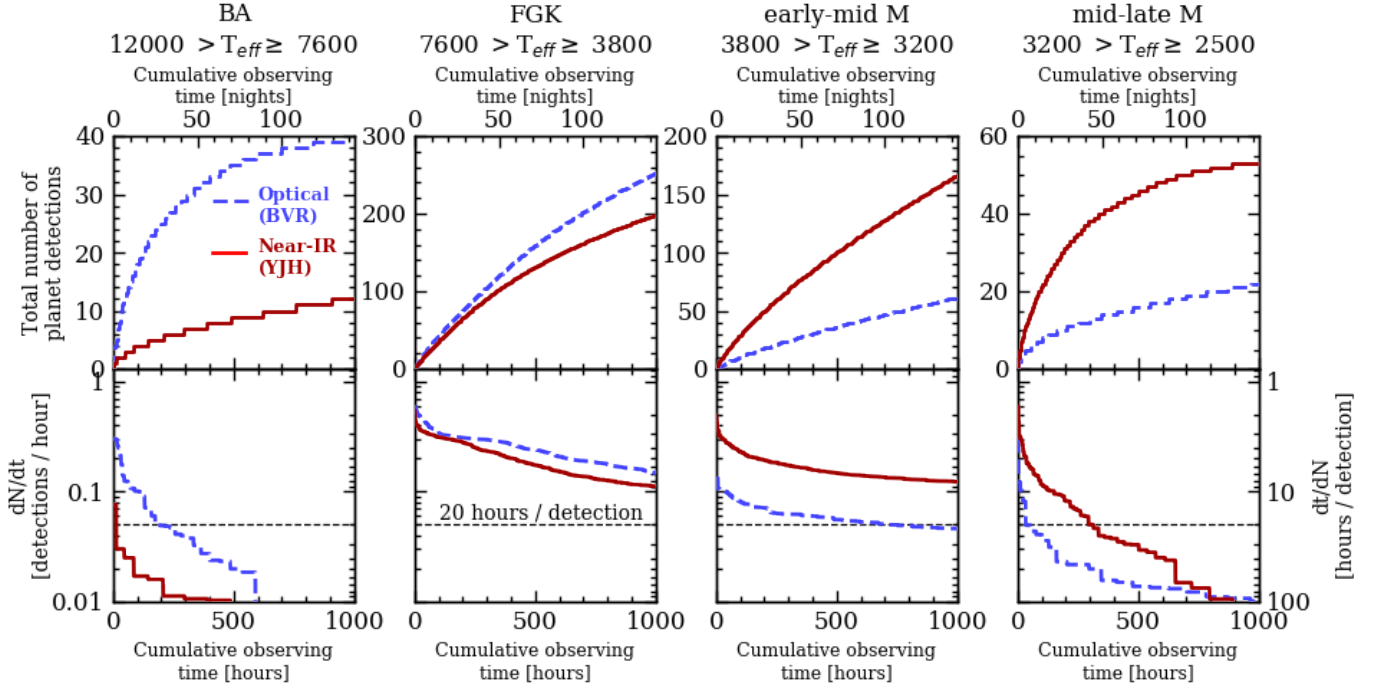


FIG. 4.— *Upper panel:* the cumulative median observing time to measure the 3σ RV masses of TESS planets as a function of host star spectral type and up to 10^3 hours. The *(dashed blue curves)* represent the results from the optical spectrograph whereas the *(solid red curves)* represent the near-IR spectrograph. *Lower panel:* the time derivative of the cumulative observing time curves used to indicate the RV planet detection efficiency. The *horizontal dashed line* highlights the value of the detection efficiency at 20 hours per detection. Note that unlike the lower panels, the upper panels do not share a common ordinate due to the differing number of planet detections around stars in each spectral type bin.

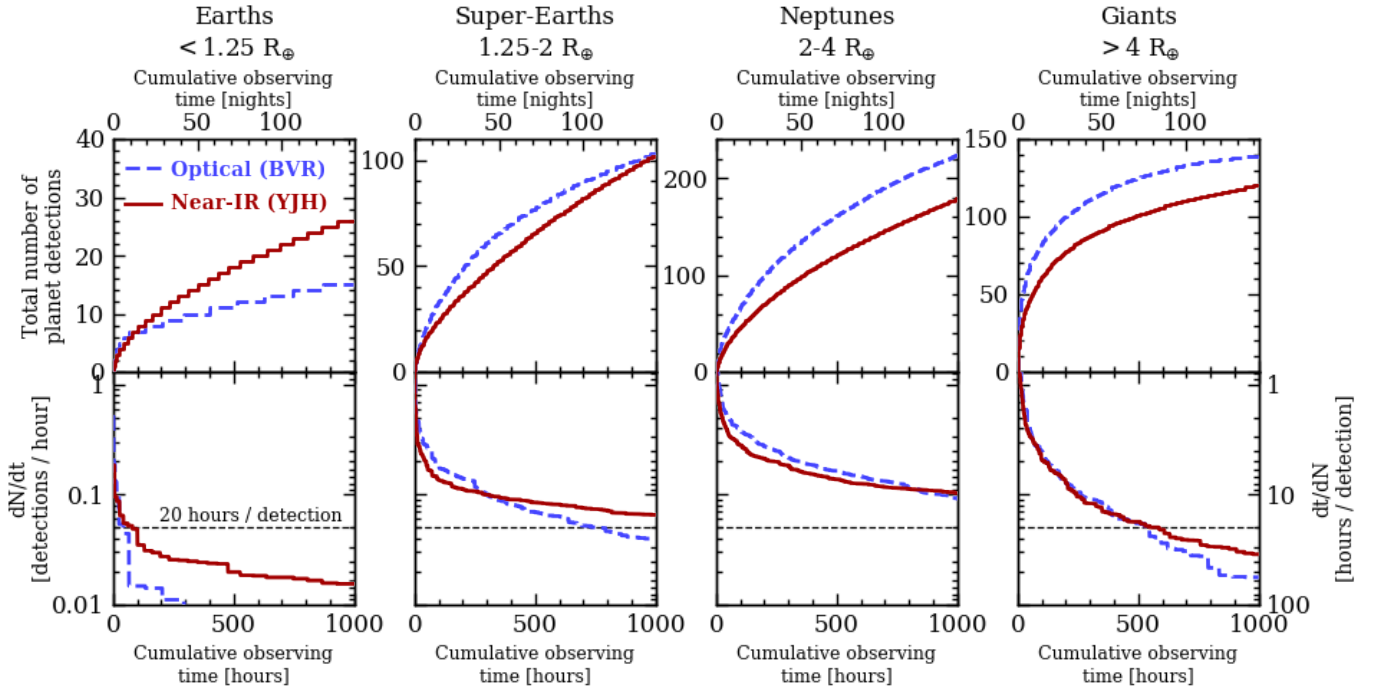


FIG. 5.— *Upper panel:* the cumulative median observing time to measure the 3σ RV masses of TESS planets as a function of planet type up to 10^3 hours. Planet type definitions are annotated above each column. The *(dashed blue curves)* represent the results from the optical spectrograph whereas the *(solid red curves)* represent the near-IR spectrograph. *Lower panel:* the time derivative of the cumulative observing time curves used to indicate the RV planet detection efficiency. The *horizontal dashed line* highlights the value of the detection efficiency at 20 hours per detection. Note that unlike the lower panels, the upper panels do not share a common ordinate due to the differing number of planet detections around stars in each spectral type bin.

clear that selecting an optimized set—in terms of shortest median observing times—of 50 small TESS planets is by far the most efficient means of characterizing their masses. Optimized target selection results in the rapid completion of the TESS level one science requirement in only ~ 60 nights with either spectrograph. The performance of the optical and near-IR spectrographs in completing the TESS level one science requirement are seen to be comparable when the ‘best’ TOIs are targeted with 31/50 being most efficiently characterized in the optical and with the remaining 19/50 being done in the near-IR. Selecting the ‘best’ 50 small planets naturally biases the sample towards larger planets with their larger K values, thus making their mass characterization faster with RVs. Despite this, the set of the ‘best’ small TESS planets with either spectrograph contains 9 super-Earths and 41 Neptunes with the average radius being $2.8 R_{\oplus}$ and the smallest planet being likely terrestrial at $1.37 R_{\oplus}$ (c.f. inset of Fig. 6).

We note that identifying the ‘best’ small TESS planets cannot be done exactly until the conclusion of the full TESS planet search. By not focusing on the ‘best’ 50 small TESS planets and instead opting to obtain RV measurements of any small planet, the total observing time required to complete the TESS level one science requirement will be longer by more than an order of magnitude on average with either spectrograph. Although the exact time allotment will depend on the exact planet sample. However the ‘best’ curves for each spectrograph in Fig. 6 are nearly indistinguishable indicating that together optical and near-IR spectrographs will readily complete the TESS level one science requirement and possibly within weeks of relevant TOIs being announced due to the low number of required RV measurements, typically $N_{\text{RV}} = 32$. Given the efficiency of measuring the ‘best’ small TESS planets at 5σ (~ 5 hours per detection), the community may opt to focus on a larger subsample of Earth-like planets or to even increase the required mass detection significance to $> 5\sigma$ thus enhancing the TESS return of planets smaller than $4 R_{\oplus}$.

5.2.1. A-priori estimate of the ‘best’ targets

Recall that identifying the optimum targets to achieve the TESS level one science requirement in the most efficient manner requires observers either to wait until the conclusion of the 2-year long TESS planet search or to select targets based on a-priori knowledge of the population of the ‘best’ small planets. The latter scenario is favorable as it allows targets to be observed with RVs almost concurrently with reported TESS detections thus leading to the shortest completion time of the TESS level one science requirement; i.e. ~ 60 nights or ~ 400 hours. Based on the predicted TESS planet population (S15) and the results of our study, we can predict the properties of the ‘best’ 50 small TESS planets and search for trends that will inform their selection throughout the actual TESS planet search. Here we suggest that identification of these planets can be done in an approximate way given some combination of intuitively crucial transit observables: the stellar magnitude, r_p , and P . The stellar magnitude constrains the photon-noise limited RV measurement precision while the latter two quantities have a direct effect on K assuming that the mass-radius relation has a positive, non-zero slope everywhere for planets

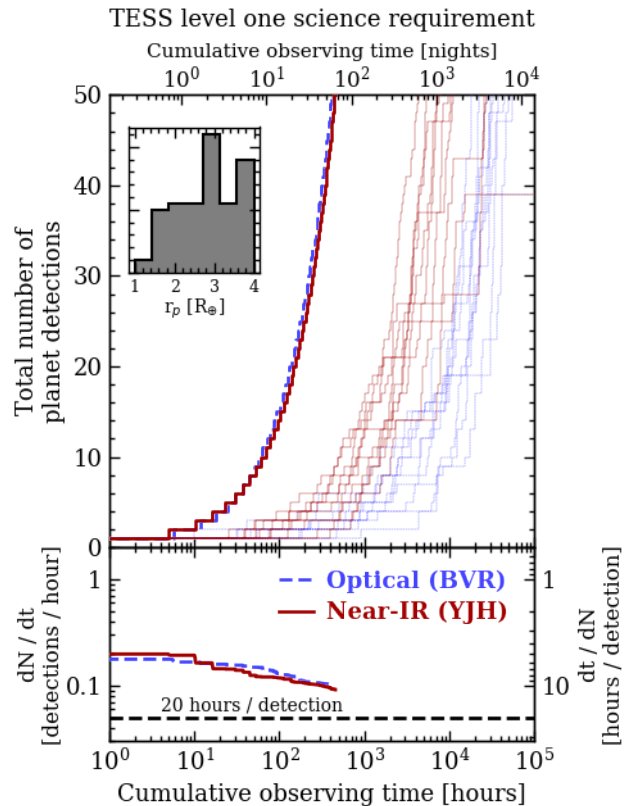


FIG. 6.— *Top panel*: the cumulative median observing time required to achieve the TESS level one science requirement of measuring the masses of 50 planets with $r_p < 4 R_{\oplus}$ at 5σ with either the optical spectrograph [dashed blue curves] or our near-IR spectrograph [solid red curves]. The set of thin curves are calculated from randomly ordered TOI samples whereas the thick curves are calculated from the sorted TOIs thus resulting in the most observationally efficient planet detections. The latter curves for each spectrograph lie almost exactly on top of each other. *Inset*: a histogram showing the joint planet radii distribution of the ‘best’ 50 TESS planets for each spectrograph. *Lower panel*: the time derivative of the thick curves shown in the upper panel. The value of the detection efficiency equal to 20 hours per detection is highlighted by the horizontal dashed line.

smaller than $4 R_{\oplus}$. After considering numerous combinations of these parameters we find that the stellar magnitude and the value of the derived-from-transit quantity $\Omega \equiv r_p^\alpha / P^{1/3}$ —for some value of α —are good diagnostics for the total observing time required to detect a transiting planet’s mass. The definition of Ω was selected to resemble the expected RV semi-amplitude K assuming a positive scaling between r_p and m_p (i.e. $\alpha > 0$) and noting that $K \propto P^{-1/3}$. In this way, large values of Ω should correspond to large K values which directly effects the observing time required to achieve a given mass detection significance as larger signals are more easily detected with a given RV measurement precision. We considered various values of $\alpha \in (0, 3]$ and found little discrepancy between these values with regards to where in the region of the corresponding magnitude- Ω parameter space the ‘best’ 50 small planets sit. Given uncertainties and possible discontinuities in the mass-radius relation for small planets we opt for $\alpha = 1$.

In Fig. 7 we compare the location of the 50 ‘best’ small planets to the remaining 1833 small planets in the apparent magnitude- Ω parameter space. For considerations

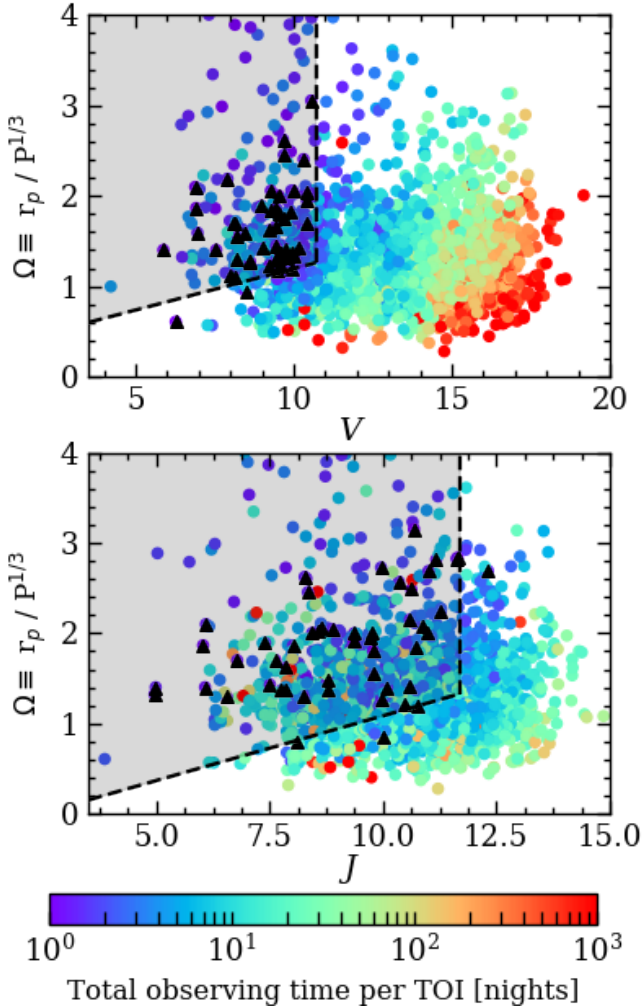


FIG. 7.— The total observing time per TOI required to detect the planet’s mass at 5σ with the optical spectrograph (*upper panel*) and the near-IR spectrograph (*lower panel*) as a function of the stellar apparent magnitude and the derived quantity from transit observables: $\Omega \equiv r_p/P^{1/3}$. The relevant apparent magnitudes for the optical and near-IR spectrographs are V and J respectively. The 50 ‘best’ TOIs with each spectrograph are designated by **black diamonds**. The **shaded regions** bounded by the *black dashed lines* approximate the regions of each parameter space with the highest likelihood of hosting planets amenable to the most efficient RV mass detections. TOIs within the shaded regions and known not to orbit an active host star should be strongly considered for rapid RV follow-up campaigns.

with our optical and near-IR spectrographs we use the V and J band magnitudes respectively. We note that in what follows we are marginalizing over stellar rotation and the level of stellar activity, both of which have a direct effect on our ability to detect planets in RV.

Unsurprisingly, the 50 ‘best’ small TESS planets are localized around bright TOIs and exhibit an increasing value of Ω with stellar magnitude. That is, as the TOIs become dimmer, a larger Ω is required for a rapid RV mass detection. To encapsulate the region of the parameter space with the highest likelihood of yielding the most efficient RV planet detections (i.e. the shortest total observing times), we truncate the outer edge of the region at a ‘maximum’ apparent magnitude and derive a lower boundary by fitting a linear function to Ω as a function of magnitude for the 50 ‘best’ small TESS plan-

ets before translating the lower boundary downwards to encapsulate 96% (i.e. 48 out of 50) of the ‘best’ small TESS planets. The resulting sets of the ‘best’ TOIs are

$$\{\text{TOIs} \mid V < 10.7, \Omega > 0.09V + 0.28\} \quad (23)$$

for follow-up with our fiducial optical spectrograph and

$$\{\text{TOIs} \mid J < 11.7, \Omega > 0.14J - 0.35\} \quad (24)$$

for follow-up with our fiducial near-IR spectrograph. These sets approximately represent the TOIs with the shortest total observing times and should be seriously considered for rapid RV follow-up observations if they are known to not orbit a rapid rotator or an overly active star. Recall that stellar rotation and activity have been marginalized over in the derivation of Eqs. 23 and 24.

5.3. Science Case 2: informing the mass-radius relation of planets across the radius valley

Accurate characterization of the empirical mass-radius relation for exoplanets (e.g. Weiss et al. 2013; Rogers 2015; Wolfgang et al. 2016) is an important step towards understanding the diversity of exoplanet compositions as well as its use as a tool in predictive studies (e.g. S15; Cloutier et al. 2017a, Cloutier et al. 2018). For example, consideration of small exoplanets ($r_p \leq 4 R_\oplus$) with masses measured to better than 20% revealed that a large fraction of planets with $r_p \lesssim 1.6 R_\oplus$ are rocky with bulk compositions consistent with that of the Earth and Venus (Dressing et al. 2015). The transition from bulk rocky compositions to less dense planets with a significant size fraction of volatile-rich envelope gas has also been shown to occur between $\sim 1.5 - 2.5 R_\oplus$ where a paucity of planets exists (Fulton et al. 2017; Van Eylen et al. 2017). The precise characterization of the mass-radius relation in the vicinity of this so-called *radius valley* will elucidate as to whether or not the valley persists in terms of planet bulk densities as the peaks in the bi-modal radius distribution are posited to harbour terrestrial and volatile-rich planets on opposing sides of the radius valley. Characterizing the mass-radius relation in this regime will greatly benefit from the inclusion of relevant TESS planets.

In order to accurately inform the mass-radius relation of planets across the radius valley with TESS planets, we seek a 20% fractional mass uncertainty (i.e. 5σ mass detection) following Dressing et al. (2015). We define TESS planets of interest as those spanning the radius valley using the period-dependent locus of planet radii—and its upper and lower bounds—as defined by the powerlaw in Van Eylen et al. (2017) from asteroseismology.

The cumulative median observing time required to detect relevant TESS planets at 5σ are shown in Fig. 8. To avoid the bias that the most efficiently observed targets have towards larger planets and correspondingly larger K on average, the ‘best’ planets in this science case are selected equally from two bins on either side of the radius valley with $r_p \leq 2$ and $> 2 R_\oplus$. There are 542 TESS planets that span the radius valley. RV mass characterization of all such planets will require $\gtrsim 5 \times 10^4$ and $\gtrsim 7000$ observing nights in the optical and near-IR respectively. Evidently, the cumulative observing time for all TESS planet across the radius valley is likely too large to complete even with all available spectrographs. Fortu-

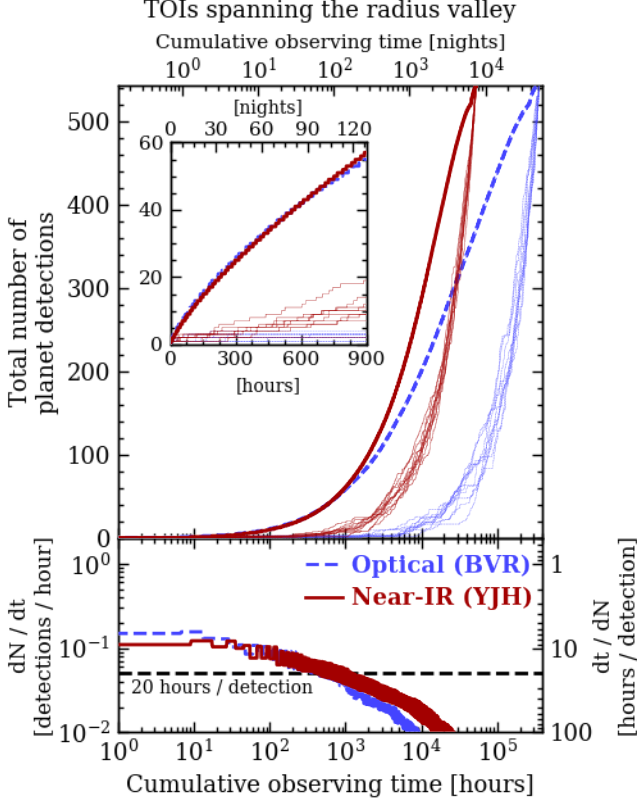


FIG. 8.— *Top panel*: the cumulative median observing time required to measure the 5σ RV masses of TESS planets spanning the radius valley ($1.5 \lesssim r_p/R_\oplus \lesssim 2.6$) with either the optical spectrograph (*dashed blue curves*) or our near-IR spectrograph (*solid red curves*). The set of thin curves are calculated from randomly ordered TOI samples whereas the thick curves are calculated from the sorted TOIs—with an equal number of planets less than and greater than $2 R_{oplus}$ —thus resulting in the most observationally efficient planet detections. *inset*: focusing on the region up to 900 cumulative observing hours (i.e. ~ 130 nights). *Lower panel*: the time derivative of the thick curves shown in the upper panel. The value of the detection efficiency equal to 20 hours per detection is highlighted by the *horizontal dashed line*.

nately, not all 542 planets are required to be measured in order to resolve the radius valley in planet bulk density. If instead we focus on the ‘best’ TESS planets then our detection efficiency with either spectrograph remains less than 20 hours per detection up to $\sim 80 - 130$ nights. In that time we expect to detect ~ 55 planets that span the radius valley with either spectrograph, if those planets are optimally chosen (c.f. Fig. 7). This implies that optical and near-IR spectrographs are equally well-suited to characterizing the ‘best’ TESS planets across the radius valley with near-IR observations only becoming more efficient after ~ 60 planet detections. With this sample of TESS planets, the hypothesized rocky/volatile-rich transition can be resolved and will help in progressing towards potentially resolving the radius/bulk density valley as a function of host spectral type.

5.4. Science Case 3: characterization of temperate Earths & super-Earths

Temperate planets that orbit close to or within their host star’s habitable zone are of particular interest for the search for life. Here we aim to scrutinize the masses of potentially habitable planets that we define herein as

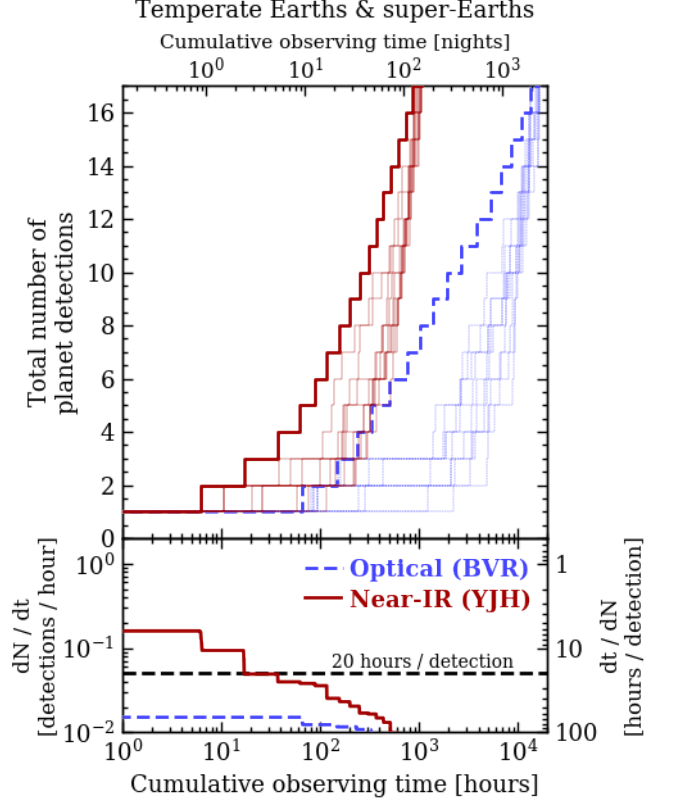


FIG. 9.— *Top panel*: the cumulative median observing time required to measure the RV masses of potentially habitable TESS planets at 3σ with either the optical spectrograph (*dashed blue curves*) or our near-IR spectrograph (*solid red curves*). Potentially habitable planets are defined as either Earths or super-Earths with $r_p \leq 2 R_\oplus$ and orbit within their host star’s habitable zone as defined by (Kopparapu et al. 2013). The set of thin curves are calculated from randomly ordered TOI samples whereas the thick curves are calculated from the sorted TOIs thus resulting in the most observationally efficient planet detections. *Lower panel*: the time derivative of the thick curves shown in the upper panel. The value of the detection efficiency equal to 20 hours per detection is highlighted by the *horizontal dashed line*.

Earths and super-Earths ($r_p \leq 2 R_\oplus$) orbiting within the habitable zone (HZ). To define the HZ we adopt the ‘water-loss’ and ‘maximum-greenhouse’ HZ limits from Kopparapu et al. (2013). There are just 17 such planets in the S15 synthetic catalog, three of which are smaller than $1.5 R_\oplus$ and are likely to be rocky. Fig. 9 depicts the cumulative median observing time required to detect the masses of potentially habitable TESS planets at 3σ . Due to TESS’s limited observational baselines, the majority of HZ TESS planets—including the full set of 17 potentially habitable TESS planets—orbit M dwarfs and thus favor near-IR RV follow-up. The cumulative observing time required to measure all potentially habitable TESS planet masses at 3σ is ~ 150 nights with the near-IR spectrograph. This is about fifteen times shorter than the total time required to complete the same task with the optical spectrograph. Regardless of the spectrograph used, RV follow-up of potentially habitable TESS planets will be an expensive task with just ~ 2 planets detected in ~ 2.5 nights after which the detection efficiency begins to require more than 20 hours per detection.

We caution that with such a small sample of potentially

habitable TESS planets that the numbers presented here regarding the cumulative observing time required to detect such planets may be misleading. Due to the small number statistics the results for temperate Earths and super-Earths are highly sensitive to the true properties of those planetary systems. For example, a potentially habitable TESS planet may be detected around an M dwarf with $J < 10.15$ —the brightest TOI with a potentially habitable planet from S15—thus resulting in a shorter total observing time required to detect one such planet with RVs.

5.5. Science Case 4: characterization of favorable JWST follow-up targets

The *James Webb Space Telescope* (JWST) to-be launched in May 2020 will revolutionize our understanding of transiting exoplanet atmospheres (see Beichman et al. 2014 for a summary of science cases). Many TOIs will represent some of the most interesting targets for atmospheric characterization with JWST through transmission spectroscopy observations in particular. To quantify the RV requirement needed to understand the bulk densities of these planets we will consider TOIs that are most amenable to efficient JWST observations. Specifically, TOIs with their expected S/N of transmission features ≥ 10 .

For each TOI we calculate the expected S/N in transmission from the expected differential transmission depth ΔD of the planet and the photon-noise per spectral bin σ_{ppm} ; $S/N = \Delta D / \sigma_{\text{ppm}}$. The value of σ_{ppm} is measured in the J -band with spectral resolution $R = 50$ (i.e. $\delta\lambda = 25$ nm), an instrumental throughput of 50%, and an integration time equal to the planet’s full transit duration. Values of ΔD for each TESS planet are computed up to five scale heights in a cloud-free atmosphere using the standard equation

$$\Delta D = 15 \text{ ppm} \left(\frac{T_p}{250 \text{ K}} \right) \left(\frac{\rho}{5.55 \text{ g/cm}^3} \right)^{-1} \left(\frac{\mu}{29 \text{ u}} \right)^{-1} \left(\frac{R_s}{0.25 R_\odot} \right)^{-2}, \quad (25)$$

where T_p is the planet’s isothermal atmospheric temperature (calculated assuming uniform heat redistribution over the planetary surface and zero albedo), ρ is the planet’s bulk density, μ is the mean molecular weight of the atmosphere, and R_s is the stellar radius. The atmospheric mean molecular weights of the TESS planets are not given in S15 so we adopt a very simplistic prescription of μ using a step-wise function of H/He-dominated atmospheres ($\mu = 2$) to Earth-like atmospheres ($\mu = 29$) for planets $\leq 2 R_\oplus$. However, this simple prescription is known to be inaccurate but an approximation is necessary to facilitate the exercise of estimating ΔD for planets yet to be studied in transmission.

According to Eq. 25 the interpretation of planetary transmission spectra heavily relies on a-priori knowledge of the planet’s bulk density. The ρ measurement precision is derived from the measurement precision on both the planet’s radius σ_{r_p} —from its TESS light curve—and on its mass measured from RVs. Due to the cubic dependence of ρ on r_p compared to its linear dependence

on m_p , improving a planet’s bulk density measurement precision is most effectively done by reducing σ_{r_p} either through more complete transit data or more precise characterization of the host stellar radius. Because of this, it is not worthwhile to sit on any TESS planet with RVs to achieve the typical mass detection significance required to precisely measure the planet’s bulk density. For example, given the photometric precision for each TOI from S15 and a notional stellar radius uncertainty of 10% (Carter et al. 2008), achieving a 3σ bulk density detection would require a $\sim 6.9\sigma$ mass detection on average. Such a precise RV mass measurement would require a $\sim 7.8\sigma$ K measurement or $(0.327/0.129)^2 = 6.4$ more observing time than a 3σ mass detection. We therefore opt for a more reasonable mass detection of 5σ , similarly to what was pursued when characterizing 50 TESS planets smaller than $4 R_\oplus$ and planets across the radius gap in Sects. 5.2 and 5.3.

Fig. 10 depicts the cumulative median observing time required to detect the 5σ masses of TESS planets that are favorable for JWST follow-up with an expected transmission $S/N \geq 10$. There are 1169 such TESS planets. By our simple prescription for ΔD for planets smaller than $2 R_\oplus$ and by imposing a minimum expected transmission $S/N \leq 10$, the sample of 1169 favourable JWST targets has been restricted to planets larger than $2 R_\oplus$ —with a median value of $r_p = 2.9 R_\oplus$ —due to their systematically larger scale heights compared to Earths and super-Earths. Detecting all 1018 Neptunes and all 151 giant planets would require $\sim 10^8$ nights with the near-IR spectrograph which is ~ 40 times shorter than the total time required using the optical spectrograph. If follow-up observations are focused on the ‘best’ subset of favorable TESS planets for JWST follow-up, then the detection efficiency of these planets remains less than 20 hours per detection for up to ~ 400 nights wherein ~ 220 planets are measured with the near-IR spectrograph. Conversely, the detection efficiency in the optical drops to 20 hours per detection slightly sooner—after ~ 360 nights but with a similar number of planet detections. Yet again spectrographs in the optical and near-IR demonstrate a comparable performance when characterizing the ‘best’ planets favorable for JWST follow-up with some slight improvement in the optical before its detection efficiency begins to drop off after ~ 360 nights. It is clear that many interesting TESS planets will be readily characterized with RVs thus providing a large sample of TESS planets with precisely characterized masses and bulk densities prior to the launch of JWST.

6. DISCUSSION AND CONCLUSIONS

We have presented calculations of the observing time required to measure the masses of the expected TESS planet population using ground-based precision radial velocities. Our calculations are based on analytical estimates (see Sect. 2) of the number of RV measurements required to detect a transiting planet’s RV semi-amplitude K at a given precision. When coupled to an exposure time calculator this yields the total observing time per target. Our main conclusions are summarized below.

1. The number of RV measurements required to detect a transiting planet’s mass is dependent on the desired K measurement precision, the rms of

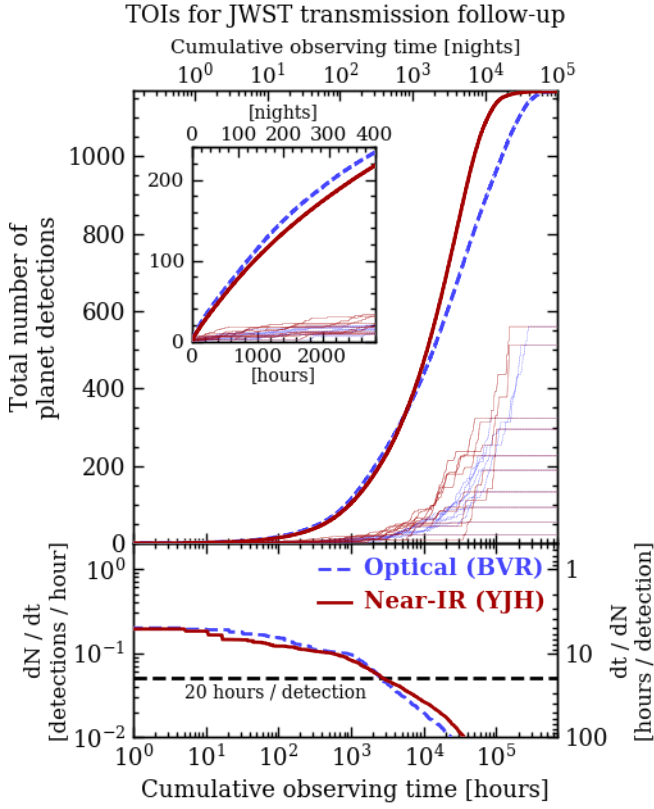


FIG. 10.— *Top panel*: the cumulative median observing time required to measure the RV masses of TESS planets favorable for follow-up transmission spectroscopy observations with JWST (i.e. transmission $S/N \geq 10$) at 5σ with either the optical spectrograph (*dashed blue curves*) or our near-IR spectrograph (*solid red curves*). The set of thin curves are calculated from randomly ordered TOI samples whereas the thick curves are calculated from the sorted TOIs thus resulting in the most observationally efficient planet detections. *inset*: focusing on the region up to ~ 2800 cumulative observing hours (i.e. ~ 400 nights). *Lower panel*: the time derivative of the thick curves shown in the upper panel. The value of the detection efficiency equal to 20 hours per detection is highlighted by the *horizontal dashed line*.

the RVs observations (this includes contributions from photon-noise, stellar activity, additional unseen planets, and systematic effects), and whether or not the residual RV noise is correlated or not. Eq. 18 can be used to calculate the number of required RV measurements if the RV residuals are uncorrelated, otherwise the formalism presented in Sect. 2.1.2 must be used.

2. Efficient characterization of transiting planet masses for a given planet type (e.g. super-Earths) favors targets with small photon-noise limited RV measurement precisions. High precision measurements are most readily achieved with optical spectral coverage (i.e. BVR bands in this study) for Sun-like stars with $T_{\text{eff}} \gtrsim 5500$ K whereas M dwarfs with $T_{\text{eff}} \lesssim 3800$ K are favored by near-IR spectrographs (i.e. YJH bands in this study).
3. Overall, the relative merits of obtaining precise RVs in the optical compared to in the near-IR are nearly equivalent. That is that RV campaigns aiming to characterize TESS planets can largely be done as

effectively in either wavelength domain with the exception of the characterization of Earths ($r_p < 1.25 R_{\oplus}$) and temperate TESS planets that are preferentially found around M dwarfs.

4. Not all TESS planets will be amenable to RV follow-up observations and selecting random TOIs for follow-up is an incredibly inefficient method of target selection. Instead, targets should be selected based on their apparent magnitude—to minimize the photon-noise limited RV precision—and the transit-derived quantity $\Omega = r_p/P^{1/3}$. The subset of TOIs belonging to either optimal set defined by Eqs. 23 and 24 should be strongly considered for immediate RV follow-up.
5. The TESS level one science requirement of measuring the masses of 50 planets with $r_p < 4 R_{\oplus}$ at the 20% level (i.e. 5σ mass detection) can be achieved in as little as ~ 400 hours or ~ 60 nights of observation.
6. ~ 55 TESS planets spanning the radius gap for small planets (i.e. $1.5 \lesssim r_p/R_{\oplus} \lesssim 2.6$) can be detected efficiently at 5σ in ~ 130 nights before the detection efficiency drops below 0.05 detections per hour (i.e. 20 hours per detection).
7. Only ~ 2 temperate super-Earths can be detected efficiently at 3σ in ~ 2.5 nights before the detection efficiency exceeds 20 hours per detection.
8. ~ 220 Neptunes and giant planets amenable to transmission spectroscopy follow-up observations with JWST can be detected efficiently with a 5σ mass detection in $\sim 360 - 400$ nights before the detection efficiency exceeds 20 hours per detection.
9. An online version of the **Radial Velocity Follow-up Calculator** used throughout this paper on the expected TESS planet population is available at <http://maestria.astro.umontreal.ca/rvfc>. This general-usage tool can be used to calculate the number of RV measurements and total observing time required to detect the RV semi-amplitude of any transiting planet to a user-defined detection significance and with a user-defined spectrograph.

The results of this paper have been based on the synthetic planet population presented in S15. In their study they reported the expected TESS planet population (i.e. ~ 1700 planets) recovered from the TESS 2 minute cadence observing mode of the brightest targets. Additionally, deeper full frame images at a 30 minute cadence will be released and result in even more planet candidates, some of which may still be amenable to RV follow-up observations. Another population of TOIs not considered in our calculations is the population of targets featuring only one or two transit-like events. If confirmed, the corresponding planets will be interesting in their own right as their orbits will have systematically longer periods making them cooler and of interest for future habitability studies. Lastly, the TESS mission has the possibility of being extended beyond its nominal 2-year long primary

mission. If extended, the extension of the TESS observational baselines will improve the measured ephemerides of confirmed TESS planets, shed light on the nature of systems exhibiting single transit-like events, and expand the population of planets discovered with TESS (see the overview in Bouma et al. 2017).

Further caveats to the planet population from S15 used throughout this study were addressed by a variety of studies and corresponding updates to the expected TESS planet population (e.g. Ballard 2018; Barclay et al. 2018). For example, Barclay et al. (2018) updated the calculations of S15 by using the TESS Candidate Target List (Stassun et al. 2017) and consequently updating the number of TESS discoveries including a decreased number of Earths and super-Earths which will have important implications for the corresponding science cases such as the bulk density characterization of TESS planets near the radius valley ($r_p \sim 2 R_\oplus$). Furthermore, Ballard (2018) predicted that the planet population around M1-M4 dwarfs was underestimated. The results imply a larger cumulative planet yield around M dwarfs including many systems with multiple transiting planets. This has important implications for RV follow-up campaigns of TOIs as M dwarf planets have the potential to be the most efficiently detected planets in radial velocity. In practice this will depend on the on-sky performance of many of the up-coming generation of near-IR velocimeters which have favorable RV measurement precision when observing M dwarfs. Many up-coming near-IR spectrographs are anticipated to operate with an RV noise floor of $\sim 1 \text{ m s}^{-1}$ comparable to many high performance optical spectrographs but this may prove challenging as demonstrated by the CARMENES near-IR channel that seems to yield lower precision ($\sim 2-3 \text{ m s}^{-1}$) on early to mid-M dwarfs compared to the sub-1 m s^{-1} performance achieved in the optical (Reiners et al. 2017, c.f. Fig 6). The focus on M dwarf planets with either class of spectrograph is well warranted as these planets represent some of the most interesting planets in terms of potential habitability and for the prospect transmission spectroscopy follow-up with JWST.

In Sect. 5.5 we presented the results for the most favorable TESS targets for transmission spectroscopy follow-

up with JWST. In addition to identifying the ‘best’ such planets based on the time required to measure their masses (i.e. bulk densities) with RVs, one may also consider metrics describing the ease of detecting atmospheric features in either transmission or thermal emission as in Kempton et al. (2018). Favorable TESS planets based on our calculations of the observing time required to detect their masses in RVs, that also overlap with favorable TESS planets based on the metrics from Kempton et al. (2018), should be strongly considered for rapid RV follow-up. Similar target selection may be done based on the simulated transmission spectra from Louie et al. (2018) and the resulting S/N in transmission.

It is worth reiterating that although TOIs will be frequently reported following the launch and commissioning of TESS, RV follow-up teams should refrain from targeting just any TOI. Many detected planets will orbit stars either too dim or too active for efficient RV characterization. We emphasize that TOIs amenable to RV follow-up can be approximately identified—in real time—if they belong to one of the sets defined in Eqs. 23 or 24, or equivalently, if they lie in one of the shaded regions of either panel in Fig. 7. However the sets of the ‘best’ TOIs are derived by marginalizing over the population of additional unseen planets in the system and the star’s intrinsic RV activity. The former source of RV signals will not be illuminated unless RV follow-up of the system commences but the level of stellar activity can be estimated from the star’s photometric variability in its TESS light curve. In addition to selecting targets based on Eqs. 23 and 24, stars with high amplitudes of photometric variability or jitter should not be considered for efficient RV follow-up campaigns.

RC thanks Raphaëlle Haywood and Jason Dittmann for useful discussions of the GP implementation, particularly for the LHS 1140 system. RC thanks the Canadian Institute for Theoretical Astrophysics for use of the Sunnyside computing cluster throughout this work. RC is partially supported in this work by the National Science and Engineering Research Council of Canada.

APPENDIX

RADIAL VELOCITY FOLLOW-UP CALCULATOR

Our models for the number of RV measurements N_{RV} required to detect a transiting planet at a given significance—in the presence of white or correlated RV noise—are generalizable to the majority transiting planets observed with any velocimeter. Recall that our models are only applicable to planets on nearly circular orbits, with known ephemerides, and whose orbital phase curves will be (approximately) uniformly sampled in the white noise case. Furthermore, because the results presented throughout this paper have been regarding a hypothetical planet population and with only two fiducial spectrographs, we present to the community an online web-tool version of the generalized *Radial Velocity Follow-up Calculator*¹⁰ (RVFC) used throughout this study.

The RVFC is intended to serve the community by providing rapid calculations of N_{RV} and total observing times for an arbitrary user-defined transiting planet with a user-defined spectrograph, given parameters of the planet from its transit light curve, stellar parameters, parameters of the employed spectrograph, RV noise parameters, and a small number of additional simulation parameters. The exact input parameters required by the calculator will depend on which of two possible primary modes-of-operation the user selects. In *option 1*, the calculator is used to calculate the photon-noise limited RV measurement precision σ_{RV} using the formalism discussed in Sect. 2.2 and PHOENIX stellar models. Two suboptions are available for users to either add additional RV noise sources which are sampled from appropriate empirical distributions (*option 1.1*) or for the user to specify verbatim those additional noise sources (*option 1.2*). In *option 2*, the user can input a fixed value of σ_{RV} thus negating the need for certain input parameters

¹⁰ <http://maestria.astro.umontreal.ca/rvfc>

TABLE 5
DESCRIPTIONS OF RVFC INPUT PARAMETERS

Parameter	Units	Required for RVFC Option(s)	Usage	Notes
<i>Spectrograph parameters</i>				
Minimum spectrograph wavelength	nm	1	Interpolating σ_{RV} .	
Maximum spectrograph wavelength	nm	1	Interpolating σ_{RV} .	
Spectral resolution, R	$\lambda/\Delta\lambda$	1	Interpolating & calculating σ_{RV} .	
Telescope aperture	m	1	Calculating σ_{RV} .	
Throughput	[0-1]	1	Calculating σ_{RV} .	
RV noise floor, σ_{floor}	m s^{-1}	1	Contributes to RV rms.	
<i>Planet parameters</i>				
Orbital period, P	days	1,2	Calculating the expected K and sampling unseen planets.	
Planetary radius, r_p	R_{\oplus}	1,2	Estimating m_p from Eq. 22 and sampling unseen planets.	
Planetary mass, m_p	M_{\oplus}	1,2	Calculating the expected K .	If unspecified, m_p is estimated from r_p and the mass-radius relation (Eq. 22).
<i>Stellar parameters</i>				
Apparent magnitude, V or J	-	1	Calculating σ_{RV} .	The spectral coverage of the spectrograph must span either V or J .
Stellar mass, M_s	M_{\odot}	1,2	Calculating the expected K , $\log g$ for σ_{RV} , sampling stellar activity, and sampling unseen planets.	
Stellar radius, R_s	R_{\odot}	1,2	Calculating $\log g$ for σ_{RV} .	
Effective temperature, T_{eff}	K	1,2	Interpolating σ_{RV} , estimating stellar colors, sampling stellar activity, and sampling unseen planets.	
Metallicity, Z	[Fe/H]	1,2	Interpolating σ_{RV} .	
Projected rotation velocity, $v \sin i_s$	km s^{-1}	1	Interpolating σ_{RV} .	
Rotation period, P_{rot}	days	1,2	Calculating σ_{RV} and sampling stellar activity	If unspecified, P_{rot} is estimated from R_s and $v \sin i_s$ assuming $\sin i_s = 1$.
<i>RV noise sources</i>				
Photon-noise limited RV precision, σ_{RV}	m s^{-1}	2	Contributes to RV rms.	
RV activity rms, σ_{act}	m s^{-1}	1,2	Contributes to RV rms.	Can be set to zero or is sampled if left unspecified.
RV rms from unseen planets, σ_{planets}	m s^{-1}	1,2	Contributes to RV rms.	Can be set to zero or is sampled if left unspecified.
Effective RV rms, σ_{eff}	m s^{-1}	2	Calculating N_{RV} .	If unspecified, σ_{eff} is computed from above contributing noise sources.
<i>Simulation parameters</i>				
Exposure time, t_{exp}	minutes	1,2	Calculating S/N and the total observing time.	
Overhead time	minutes	1,2	Calculating σ_{RV} .	
Desired K detection significance, K/σ_K	-	1,2	Calculating N_{RV} .	
Number of GP trials, N_{GP}	-	1,2	Calculating N_{RV} in the presence of red noise.	If zero, only do the white noise calculation. If $N_{\text{GP}} > 0$ then we recommend setting $N_{\text{GP}} \gtrsim 10$ for decent sampling. Value returned is the median of all trials if $N_{\text{GP}} \geq 2$.

to be specified by the user and speeding up the wall time of the calculation. *Option 2* also features the two suboptions available for *option 1* and additionally has a third option in which the effective RV rms (i.e. the combination of all RV noise sources) is set verbatim if its value is known for the system of interest and only white noise calculations are desired (*option 2.3*). *Option 2* may be viable for users whose employed spectrograph features an independent ETC, the results from which differ from those returned by the built-in RVFC ETC. The input parameters required to run the RVFC are summarized in Table 5.

One notable bottleneck in the wall-time of running the RVFC is the time required to compute the photon-noise limited RV precision given a unique set of stellar and spectrograph parameters. To facilitate *rapid* calculations with the RVFC we opt to interpolate these values from pre-computed tables rather than perform the calculations explicitly. The tables from which σ_{RV} values are interpolated from are computed individually for each of the spectral bands shown in Table 1 and over five additional parameters: the spectral resolution, T_{eff} , $\log g$, Z , and $v \sin i_s$. Given values for these parameters in the RVFC, the corresponding σ_{RV} is obtained by interpolating over this grid for each spectral band spanned by the spectrograph's wavelength domain. The remaining spectrograph parameters and stellar magnitude are then used to scale the interpolated value of σ_{RV} to the correct S/N per resolution element. Notably, the interpolation of σ_{RV} necessitates a trade-off between accuracy and computing time. However, the loss in accuracy we deem acceptable given the often inexact values of the other sources of RV noise (i.e. instrument stability, activity, and additional unseen planets).

Lastly, recall that the RVFC can calculate N_{RV} in either white or correlated RV noise limits according to our models discussed in Sects. 2.1.1 and 2.1.2 respectively. As noted in Sect. 2.1.2, the results in the latter scenario are dependent on the time-sampling which has been sampled uniformly in this study over a fixed baseline. This is also adopted in the initial version of the RVFC. As such, for users interested in calculating N_{RV} in the presence of correlated RV noise we recommend using multiple calculations (e.g. $N_{\text{GP}} \gtrsim 10$) to obtain the most-likely value and spread in N_{RV} given a suite of sampled window functions. Users beware that increasing N_{GP} will require a correspondingly longer computation time. In the future we would like to implement a way for users to upload custom window functions to avoid this ambiguity.

FISHER INFORMATION WITH A QUASI-PERIODIC GAUSSIAN PROCESS REGRESSION MODEL

Here we derive the Fisher information matrix terms for a circular keplerian RV model plus a quasi-periodic GP correlated noise activity model, including an additional scalar jitter parameter. As discussed in Sect. 2.1.2 the keplerian model parameter is solely the RV semi-amplitude $\{K\}$ whilst the GP covariance model has five hyperparameters $\Theta = \{a, \lambda, \Gamma, P_{\text{GP}}, \sigma_{\text{jitter}}\}$ that describe the quasi-periodic covariance matrix C commonly used when simultaneously fitting RV planets and stellar activity:

$$k_{ij} = a^2 \exp \left[-\frac{(t_i - t_j)^2}{2\lambda^2} - \Gamma^2 \sin^2 \left(\frac{\pi|t_i - t_j|}{P_{\text{GP}}} \right) \right], \quad (\text{B1})$$

$$C_{ij} = k_{ij} + \delta_{ij} \sigma_{\text{RV},i}^2. \quad (\text{B2})$$

We therefore have six model parameters leading to a 6×6 Fisher information matrix B which is related the model parameter covariance matrix $C' = B^{-1}$ from which model parameter measurement uncertainties are calculated. Assuming a circular keplerian orbit for the transiting planet of interest, the residual RV vector is

$$\mathbf{r}(\mathbf{t}) = \mathbf{y}(\mathbf{t}) - (-K \sin(\phi(\mathbf{t}))) \quad (\text{B3})$$

where \mathbf{y} are the raw RVs observed at times \mathbf{t} and $\phi(\mathbf{t})$ is the planet's orbital phase centered on mid-transit. The generalized lnlikelihood from which the Fisher information matrix is calculated is then

$$\ln \mathcal{L} = -\frac{1}{2} (\mathbf{r}^T C^{-1} \mathbf{r} + \ln \det C + \text{constant}), \quad (\text{B4})$$

Before populating the Fisher information matrix, we note two crucial mathematical identities

$$\frac{\partial}{\partial \theta} C^{-1} = -C^{-1} \frac{\partial C}{\partial \theta} C^{-1}, \quad (\text{B5})$$

$$\frac{\partial}{\partial \theta} \ln \det C = \text{tr} \left(C^{-1} \frac{\partial C}{\partial \theta} \right). \quad (\text{B6})$$

We can now proceed with calculating the general equation for each of the 21 unique Fisher information matrix entries in terms of partial derivatives of either the RV residual vector or covariance matrix C with respect to the model parameters instead of the partial derivative of the inverse covariance matrix.

$$B_{ij} = -\frac{\partial^2 \ln \mathcal{L}}{\partial \theta_i \partial \theta_j}, \quad (\text{B7})$$

$$\begin{aligned} \frac{\partial \ln \mathcal{L}}{\partial \theta_i} &= \frac{\partial}{\partial \theta_i} \left[-\frac{1}{2} \mathbf{r}^T C^{-1} \mathbf{r} - \frac{1}{2} \ln \det C \right] \\ &= -\frac{1}{2} \left[\left(\frac{\partial \mathbf{r}}{\partial \theta_i} \right)^T C^{-1} \mathbf{r} - \mathbf{r}^T C^{-1} \frac{\partial C}{\partial \theta_i} C^{-1} \mathbf{r} + \mathbf{r}^T C^{-1} \left(\frac{\partial \mathbf{r}}{\partial \theta_i} \right) + \text{tr} \left(C^{-1} \frac{\partial C}{\partial \theta_i} \right) \right], \end{aligned} \quad (\text{B8})$$

$$\begin{aligned} \frac{\partial^2 \ln \mathcal{L}}{\partial \theta_i \partial \theta_j} &= -\frac{1}{2} \left[\left(\frac{\partial^2 \mathbf{r}}{\partial \theta_i \partial \theta_j} \right)^T C^{-1} \mathbf{r} - \left(\frac{\partial \mathbf{r}}{\partial \theta_i} \right)^T C^{-1} \frac{\partial C}{\partial \theta_j} C^{-1} \mathbf{r} + \left(\frac{\partial \mathbf{r}}{\partial \theta_i} \right)^T C^{-1} \left(\frac{\partial \mathbf{r}}{\partial \theta_j} \right) \right. \\ &\quad - \left(\left(\frac{\partial \mathbf{r}}{\partial \theta_j} \right)^T C^{-1} \frac{\partial C}{\partial \theta_i} C^{-1} \mathbf{r} - \mathbf{r}^T C^{-1} \frac{\partial C}{\partial \theta_j} C^{-1} \frac{\partial C}{\partial \theta_i} C^{-1} \mathbf{r} + \mathbf{r}^T C^{-1} \frac{\partial^2 C}{\partial \theta_i \partial \theta_j} C^{-1} \mathbf{r} \right. \\ &\quad \left. \left. - \mathbf{r}^T C^{-1} \frac{\partial C}{\partial \theta_i} C^{-1} \frac{\partial C}{\partial \theta_j} C^{-1} \mathbf{r} + \mathbf{r}^T C^{-1} \frac{\partial C}{\partial \theta_i} C^{-1} \left(\frac{\partial \mathbf{r}}{\partial \theta_j} \right) \right) \right. \\ &\quad \left. + \left(\frac{\partial \mathbf{r}}{\partial \theta_j} \right)^T C^{-1} \frac{\partial \mathbf{r}}{\partial \theta_i} - \mathbf{r}^T C^{-1} \frac{\partial C}{\partial \theta_j} C^{-1} \frac{\partial \mathbf{r}}{\partial \theta_i} + \mathbf{r}^T C^{-1} \frac{\partial^2 \mathbf{r}}{\partial \theta_i \partial \theta_j} \right] \end{aligned} \quad (\text{B9})$$

Each matrix entry is calculated using Eq. B9. In Eq. B9 there are two first order and two second order partial derivatives that must be computed with respect to each of the six model parameters: $\Theta = \{K, a, \lambda, \Gamma, P_{\text{GP}}, \sigma_{\text{jitter}}\}$. These being

$$\frac{\partial \mathbf{r}}{\partial \theta_i}, \frac{\partial K}{\partial \theta_i}, \frac{\partial^2 \mathbf{r}}{\partial \theta_i \partial \theta_j}, \text{ and } \frac{\partial^2 K}{\partial \theta_i \partial \theta_j} \quad (\text{B10})$$

and can be computed analytically or symbolically using the open-source `sympy` package in `python` given the analytical expressions for the residual vector (Eq. B3) and the covariance matrix (Eq. B1 & B2).

REFERENCES

- Allen, L. E., Wright, J., Rajagopal, J., et al. 2018, in American Astronomical Society Meeting Abstracts, Vol. 231, American Astronomical Society Meeting Abstracts, 246.08
- Artigau, É., Malo, L., Doyon, R., et al. 2018, ArXiv e-prints, arXiv:1803.07646
- Artigau, É., Kouach, D., Donati, J.-F., et al. 2014, in Society of Photo-Optical Instrumentation Engineers (SPIE) Conference Series, Vol. 9147, Society of Photo-Optical Instrumentation Engineers (SPIE) Conference Series, 15
- Astudillo-Defru, N., Delfosse, X., Bonfils, X., et al. 2017a, A&A, 600, A13
- Astudillo-Defru, N., Forveille, T., Bonfils, X., et al. 2017b, A&A, 602, A88
- Ballard, S. 2018, ArXiv e-prints, arXiv:1801.04949
- Barclay, T., Pepper, J., & Quintana, E. V. 2018, ArXiv e-prints, arXiv:1804.05050
- Barnes, R., & Greenberg, R. 2006, ApJ, 647, L163
- Bastien, F. A., Stassun, K. G., Basri, G., & Pepper, J. 2013, Nature, 500, 427
- Bastien, F. A., Stassun, K. G., Pepper, J., et al. 2014, AJ, 147, 29
- Beichman, C., Benneke, B., Knutson, H., et al. 2014, PASP, 126, 1134
- Berta-Thompson, Z. K., Irwin, J., Charbonneau, D., et al. 2015, Nature, 527, 204
- Bertaux, J. L., Lallement, R., Ferron, S., Boonne, C., & Bodichon, R. 2014, A&A, 564, A46
- Bonfils, X., Delfosse, X., Udry, S., et al. 2013, A&A, 549, A109
- Bouchy, F., Pepe, F., & Queloz, D. 2001, A&A, 374, 733
- Bouchy, F., Udry, S., Mayor, M., et al. 2005, A&A, 444, L15
- Bouchy, F., Doyon, R., Artigau, É., et al. 2017, The Messenger, 169, 21
- Bouma, L. G., Winn, J. N., Kosiarek, J., & McCullough, P. R. 2017, ArXiv e-prints, arXiv:1705.08891
- Burke, C. J., McCullough, P. R., Valenti, J. A., et al. 2007, ApJ, 671, 2115
- Carter, J. A., Yee, J. C., Eastman, J., Gaudi, B. S., & Winn, J. N. 2008, ApJ, 689, 499
- Cegla, H. M., Stassun, K. G., Watson, C. A., Bastien, F. A., & Pepper, J. 2014, ApJ, 780, 104
- Chakraborty, A., Richardson, E. H., & Mahadevan, S. 2008, in Proc. SPIE, Vol. 7014, Ground-based and Airborne Instrumentation for Astronomy II, 70144G
- Charbonneau, D., Berta, Z. K., Irwin, J., et al. 2009, Nature, 462, 891
- Christiansen, J. L., Vanderburg, A., Burt, J., et al. 2017, AJ, 154, 122
- Claudi, R., Benatti, S., Carleo, I., et al. 2016, in Proc. SPIE, Vol. 9908, Ground-based and Airborne Instrumentation for Astronomy VI, 99081A
- Cloutier, R., Doyon, R., Menou, K., et al. 2017a, AJ, 153, 9
- Cloutier, R., Astudillo-Defru, N., Doyon, R., et al. 2017b, A&A, 608, A35
- Cloutier, R., Artigau, É., Delfosse, X., et al. 2018, AJ, 155, 93
- Cosentino, R., Lovis, C., Pepe, F., et al. 2012, in Proc. SPIE, Vol. 8446, Ground-based and Airborne Instrumentation for Astronomy IV, 84461V
- Crane, J. D., Shectman, S. A., Butler, R. P., et al. 2010, in Proc. SPIE, Vol. 7735, Ground-based and Airborne Instrumentation for Astronomy III, 773553
- Crause, L. A., Sharples, R. M., Bramall, D. G., et al. 2014, in Proc. SPIE, Vol. 9147, Ground-based and Airborne Instrumentation for Astronomy V, 91476T
- Crepp, J. R., Crass, J., King, D., et al. 2016, in Proc. SPIE, Vol. 9908, Ground-based and Airborne Instrumentation for Astronomy VI, 990819
- Delfosse, X., Forveille, T., Ségransan, D., et al. 2000, A&A, 364, 217
- Delfosse, X., Bonfils, X., Forveille, T., et al. 2013, A&A, 553, A8
- Dittmann, J. A., Irwin, J. M., Charbonneau, D., et al. 2017, Nature, 544, 333

- Dressing, C. D., & Charbonneau, D. 2015, *ApJ*, 807, 45
- Dressing, C. D., Charbonneau, D., Dumusque, X., et al. 2015, *ApJ*, 800, 135
- Dumusque, X., Udry, S., Lovis, C., Santos, N. C., & Monteiro, M. J. P. F. G. 2011, *A&A*, 525, A140
- Figueira, P., Adibekyan, V. Z., Oshagh, M., et al. 2016, *A&A*, 586, A101
- Forveille, T., Bonfils, X., Delfosse, X., et al. 2009, *A&A*, 493, 645
- Fressin, F., Torres, G., Charbonneau, D., et al. 2013, *ApJ*, 766, 81
- Fulton, B. J., & Petigura, E. A. 2018, *ArXiv e-prints*, arXiv:1805.01453
- Fulton, B. J., Petigura, E. A., Howard, A. W., et al. 2017, *AJ*, 154, 109
- Fűrész, G., Simcoe, R., Barnes, S. I., et al. 2016, in *Proc. SPIE*, Vol. 9908, *Ground-based and Airborne Instrumentation for Astronomy VI*, 990814
- Gaudi, B. S., & Winn, J. N. 2007, *ApJ*, 655, 550
- Ge, J., Ma, B., Sithajan, S., et al. 2016, in *Proc. SPIE*, Vol. 9908, *Ground-based and Airborne Instrumentation for Astronomy VI*, 990861
- Gibson, S. R., Howard, A. W., Marcy, G. W., et al. 2016, in *Proc. SPIE*, Vol. 9908, *Ground-based and Airborne Instrumentation for Astronomy VI*, 990870
- Gray, D. F. 2008, *The Observation and Analysis of Stellar Photospheres*
- Grunblatt, S. K., Howard, A. W., & Haywood, R. D. 2015, *ApJ*, 808, 127
- Hall, J. C., Lockwood, G. W., & Skiff, B. A. 2007, *AJ*, 133, 862
- Haywood, R. D., Collier Cameron, A., Queloz, D., et al. 2014, *MNRAS*, 443, 2517
- Henry, T. J., Soderblom, D. R., Donahue, R. A., & Baliunas, S. L. 1996, *AJ*, 111, doi:10.1086/117796
- Howard, A. W., Johnson, J. A., Marcy, G. W., et al. 2011, *ApJ*, 730, 10
- Howard, A. W., Sanchis-Ojeda, R., Marcy, G. W., et al. 2013, *Nature*, 503, 381
- Huélamo, N., Figueira, P., Bonfils, X., et al. 2008, *A&A*, 489, L9
- Husser, T.-O., Wende-von Berg, S., Dreizler, S., et al. 2013, *A&A*, 553, A6
- Isaacson, H., & Fischer, D. 2010, *ApJ*, 725, 875
- Jurgenson, C., Fischer, D., McCracken, T., et al. 2016, in *Proc. SPIE*, Vol. 9908, *Ground-based and Airborne Instrumentation for Astronomy VI*, 99086T
- Kempton, E. M.-R., Bean, J. L., Louie, D. R., et al. 2018, *ArXiv e-prints*, arXiv:1805.03671
- Knutson, H. A., Fulton, B. J., Montet, B. T., et al. 2014, *ApJ*, 785, 126
- Kopparapu, R. K., Ramirez, R., Kasting, J. F., et al. 2013, *ApJ*, 765, 131
- Kotani, T., Tamura, M., Suto, H., et al. 2014, in *Proc. SPIE*, Vol. 9147, *Ground-based and Airborne Instrumentation for Astronomy V*, 914714
- López-Morales, M., Haywood, R. D., Coughlin, J. L., et al. 2016, *AJ*, 152, 204
- Louie, D. R., Deming, D., Albert, L., et al. 2018, *PASP*, 130, 044401
- Lovis, C., Mayor, M., Bouchy, F., et al. 2005, *A&A*, 437, 1121
- Lovis, C., Dumusque, X., Santos, N. C., et al. 2011, *ArXiv e-prints*, arXiv:1107.5325
- Mahadevan, S., Ramsey, L., Bender, C., et al. 2012, in *Proc. SPIE*, Vol. 8446, *Ground-based and Airborne Instrumentation for Astronomy IV*, 84461S
- Mahmud, N. I., Crockett, C. J., Johns-Krull, C. M., et al. 2011, *ApJ*, 736, 123
- Martín, E. L., Guenther, E., Zapatero Osorio, M. R., Bouy, H., & Wainscoat, R. 2006, *ApJ*, 644, L75
- Mayor, M., Pepe, F., Queloz, D., et al. 2003, *The Messenger*, 114, 20
- Morton, T. D., Bryson, S. T., Coughlin, J. L., et al. 2016, *ApJ*, 822, 86
- Moutou, C., Hébrard, E. M., Morin, J., et al. 2017, *MNRAS*, 472, 4563
- Newton, E. R., Irwin, J., Charbonneau, D., et al. 2016, *ApJ*, 821, 93
- Noguchi, K., Ando, H., Izumiura, H., et al. 1998, in *Proc. SPIE*, Vol. 3355, *Optical Astronomical Instrumentation*, ed. S. D'Odorico, 354–362
- Noyes, R. W., Hartmann, L. W., Baliunas, S. L., Duncan, D. K., & Vaughan, A. H. 1984, *ApJ*, 279, 763
- Oliva, E., Origlia, L., Baffa, C., et al. 2006, in *Proc. SPIE*, Vol. 6269, *Society of Photo-Optical Instrumentation Engineers (SPIE) Conference Series*, 626919
- Oshagh, M., Santos, N. C., Figueira, P., et al. 2017, *A&A*, 606, A107
- Pepe, F. A., Cristiani, S., Rebolo Lopez, R., et al. 2010, in *Proc. SPIE*, Vol. 7735, *Ground-based and Airborne Instrumentation for Astronomy III*, 77350F
- Perruchot, S., Bouchy, F., Chazelas, B., et al. 2011, in *Society of Photo-Optical Instrumentation Engineers (SPIE) Conference Series*, Vol. 8151, *Society of Photo-Optical Instrumentation Engineers (SPIE) Conference Series*, 15
- Pizzolato, N., Maggio, A., Micela, G., Sciortino, S., & Ventura, P. 2003, *A&A*, 397, 147
- Prato, L., Huerta, M., Johns-Krull, C. M., et al. 2008, *ApJ*, 687, L103
- Quirrenbach, A., Amado, P. J., Caballero, J. A., et al. 2014, in *Proc. SPIE*, Vol. 9147, *Ground-based and Airborne Instrumentation for Astronomy V*, 91471F
- Rayner, J., Bond, T., Bonnet, M., et al. 2012, in *Proc. SPIE*, Vol. 8446, *Ground-based and Airborne Instrumentation for Astronomy IV*, 84462C
- Reiners, A., Bean, J. L., Huber, K. F., et al. 2010, *ApJ*, 710, 432
- Reiners, A., Shulyak, D., Anglada-Escudé, G., et al. 2013, *A&A*, 552, A103
- Reiners, A., Zechmeister, M., Caballero, J. A., et al. 2017, *ArXiv e-prints*, arXiv:1711.06576
- Ricker, G. R., Winn, J. N., Vanderspek, R., et al. 2015, *Journal of Astronomical Telescopes, Instruments, and Systems*, 1, 014003
- Rogers, L. A. 2015, *ApJ*, 801, 41
- Saar, S. H., Hatzes, A., Cochran, W., & Paulson, D. 2003, in *Cambridge Workshop on Cool Stars, Stellar Systems, and the Sun*, Vol. 12, *The Future of Cool-Star Astrophysics: 12th Cambridge Workshop on Cool Stars, Stellar Systems, and the Sun*, ed. A. Brown, G. M. Harper, & T. R. Ayres, 694–698
- Santos, N. C., Mayor, M., Naef, D., et al. 2000, *A&A*, 361, 265
- Seifahrt, A., Bean, J. L., Stürmer, J., et al. 2016, in *Proc. SPIE*, Vol. 9908, *Ground-based and Airborne Instrumentation for Astronomy VI*, 990818
- Siverd, R. J., Brown, T. M., Hygelund, J., et al. 2016, in *Proc. SPIE*, Vol. 9908, *Ground-based and Airborne Instrumentation for Astronomy VI*, 99086X
- Sliski, D., Blake, C., Johnson, J. A., et al. 2017, in *American Astronomical Society Meeting Abstracts*, Vol. 229, *American Astronomical Society Meeting Abstracts #229*, 146.09
- Sliski, D. H., & Kipping, D. M. 2014, *ApJ*, 788, 148
- Stassun, K. G., Oelkers, R. J., Pepper, J., et al. 2017, *ArXiv e-prints*, arXiv:1706.00495
- Strassmeier, K. G., Ilyin, I., Järvinen, A., et al. 2015, *Astronomische Nachrichten*, 336, 324
- Sullivan, P. W., Winn, J. N., Berta-Thompson, Z. K., et al. 2015, *ApJ*, 809, 77
- Swift, J. J., Bottom, M., Johnson, J. A., et al. 2015, *Journal of Astronomical Telescopes, Instruments, and Systems*, 1, 027002
- Szentgyorgyi, A., Baldwin, D., Barnes, S., et al. 2016, in *Proc. SPIE*, Vol. 9908, *Ground-based and Airborne Instrumentation for Astronomy VI*, 990822
- Tal-Or, L., Zechmeister, M., Reiners, A., et al. 2018, *ArXiv e-prints*, arXiv:1803.02338
- Torres, G., Andersen, J., & Giménez, A. 2010, *A&A Rev.*, 18, 67
- Van Eylen, V., Agentoft, C., Lundkvist, M. S., et al. 2017, *ArXiv e-prints*, arXiv:1710.05398
- Vanderburg, A., Montet, B. T., Johnson, J. A., et al. 2015, *ApJ*, 800, 59
- Vogt, S. S., Allen, S. L., Bigelow, B. C., et al. 1994, in *Proc. SPIE*, Vol. 2198, *Instrumentation in Astronomy VIII*, ed. D. L. Crawford & E. R. Craine, 362
- Vogt, S. S., Radovan, M., Kibrick, R., et al. 2014, *PASP*, 126, 359
- Weiss, L. M., & Marcy, G. W. 2014, *ApJ*, 783, L6
- Weiss, L. M., Marcy, G. W., Rowe, J. F., et al. 2013, *ApJ*, 768, 14
- Weiss, L. M., Rogers, L. A., Isaacson, H. T., et al. 2016, *ApJ*, 819, 83
- West, A. A., Weisenburger, K. L., Irwin, J., et al. 2015, *ApJ*, 812, 3
- Wolfgang, A., Rogers, L. A., & Ford, E. B. 2016, *ApJ*, 825, 19

Wright, J. T., Marcy, G. W., Butler, R. P., & Vogt, S. S. 2004,
ApJS, 152, 261

TABLE 6
 STELLAR PARAMETERS FROM THE S15 SYNTHETIC CATALOG

TOI	α [deg]	δ [deg]	P [days]	m_p [M_{\oplus}]	K [m s^{-1}]	S [S_{\oplus}]	M_s [M_{\odot}]	T_{eff} [K]	Distance [pc]	B	V	R	Y	J	H	$\text{med}(v \sin i_s)$ [km s^{-1}]
0000	0.44	45.22	9.135	8.19	2.03	361.7	1.40	6531	100.0	8.87	8.47	8.24	7.80	7.63	7.46	2.17
0001	0.48	-66.20	14.200	5.57	3.11	2.1	0.33	3426	60.3	16.52	15.08	14.17	12.05	11.56	10.96	0.23
0002	0.65	42.94	4.957	4.51	1.66	235.0	1.05	5546	97.7	10.86	10.12	9.72	9.09	8.81	8.46	3.24
0003	0.92	-26.07	2.160	4.32	1.95	1240.0	1.17	5984	53.7	8.61	8.06	7.76	7.20	6.98	6.73	5.81
0004	1.31	-24.95	9.753	5.81	2.95	5.9	0.46	3622	66.1	15.59	14.19	13.32	11.47	10.99	10.34	0.57
0005	1.38	10.61	13.990	5.89	3.32	2.1	0.33	3425	58.9	16.48	15.04	14.13	12.01	11.52	10.92	0.18
0006	1.78	-71.93	8.420	8.15	5.23	4.5	0.35	3444	70.8	16.73	15.29	14.38	12.28	11.79	11.19	0.27
0007	1.79	-9.14	5.618	7.03	9.15	2.6	0.15	3228	23.4	16.63	15.05	13.98	11.66	11.13	10.63	0.09
0008	1.95	-17.00	1.344	37.81	16.03	10160.0	1.63	6668	100.0	7.78	7.51	7.37	6.83	6.72	6.63	8.19
0009	2.17	-15.53	17.140	11.57	2.10	341.2	1.63	6668	100.0	7.78	7.51	7.37	6.83	6.72	6.63	7.54

NOTE. — Only a portion of this table is shown here to demonstrate its form and content. A machine-readable version of the full table is available.

TABLE 7
 MEDIAN RADIAL VELOCITY NOISE SOURCES AND FOLLOW-UP CALCULATIONS FOR 3σ PLANET MASS DETECTIONS
 OF THE S15 SYNTHETIC CATALOG

TOI	$\sigma_{\text{RV,opt}}$ [m s ⁻¹]	$\sigma_{\text{RV,nIR}}$ [m s ⁻¹]	σ_{act} [m s ⁻¹]	σ_{planets} [m s ⁻¹]	$\sigma_{\text{eff,opt}}$ [m s ⁻¹]	$\sigma_{\text{eff,nIR}}$ [m s ⁻¹]	$N_{\text{RV,opt}}$	$N_{\text{RV,nIR}}$	$t_{\text{obs,opt}}$ [nights]	$t_{\text{obs,nIR}}$ [nights]
0000	1.02	3.14	1.25	0.00	1.61	3.59	14.8	67.6	0.4	1.6
0001	10.18	8.21	7.84	2.00	13.06	11.62	294.1	159.1	42.0	3.8
0002	2.30	3.74	0.97	0.00	2.41	3.96	57.8	155.7	1.4	3.7
0003	1.09	2.77	15.11	0.00	15.16	15.41	87.2	125.7	2.1	3.0
0004	4.15	6.06	8.15	0.77	9.22	10.33	66.9	115.2	8.7	2.7
0005	9.94	8.04	7.56	1.18	12.62	11.17	241.4	111.2	34.5	2.6
0006	11.55	9.33	7.64	1.21	14.40	12.60	128.4	69.8	18.3	1.7
0007	8.99	6.69	7.93	3.37	12.86	11.30	34.6	32.0	4.9	0.8
0008	0.97	4.43	0.10	0.00	2.11	5.47	19.8	20.0	0.5	0.5
0009	0.91	4.11	0.76	0.00	1.78	4.85	14.8	108.5	0.4	2.6

NOTE. — The resulting number of RV measurements and total observing times reported here are computed in the general case of RVs in the presence of correlated noise (see Sect. 2.1.2). Only a portion of this table is shown here to demonstrate its form and content. A machine-readable version of the full table is available.